Directed self-assembly of block copolymers on chemically nano-patterned surfaces

Memòria presentada per optar al títol de Doctor en Ciència de Materials

Departament de Química

Universitat Autònoma de Barcelona

Laura Evangelio Araujo

DIRECTORS

Francesc Pérez Murano

Institut de Microelectrònica de Barcelona (IMB-CNM, CSIC)

Jordi Fraxedas Calduch

Institut Català de Nanociència i Nanotecnologia (ICN2)

TUTOR

Joan Bausells Roigé

Institut de Microelectrònica de Barcelona (IMB-CNM, CSIC)

2017

Chapter 6

Characterization of block copolymer and chemical guiding patterns using synchrotron radiation

In chemical epitaxy DSA it is very important to accurately determine the interactions that take place between the block copolymer domains and the boundaries of the guiding patterns, in order to ascertain the optimal alignment conditions for each chemical epitaxy case. On the other hand, it is also important to determine the BCP morphology and specifications depending on the processing conditions.

In this chapter, the chemical configuration and morphology of different BCPs systems are studied by means of the synchrotron radiation-based X-ray characterization techniques HAXPES (Hard X-ray Photoelectron Spectroscopy) and GISAXS.

6.1. Chemical guiding pattern characterization by X-Ray photoemission techniques

In chemical epitaxy DSA, as demonstrated in *chapter 3*, the interfacial energies between each domain of the copolymer and the chemically patterned surfaces strongly influence the final morphology and microdomain ordering. Therefore, an accurate control of the surface chemistry is needed. Ideally, the background surface should be slightly attractive to one of the BCP domains, and the chemically modified areas should be slightly affine to the other one. Within this framework, to chemically identify the nature of the different surfaces and interfaces, a high-sensitivity characterization method based on photoemission technique has been used.

One technique especially suited for the characterization of buried interfaces is HAXPES.[1] Photoemission is a well-known technique which provides information on the electronic structure of surfaces (identification of elements and their chemical state). Its high sensitivity arises from the small mean free path of the out-coming photoelectrons in solid matter. Using conventional excitation sources with discrete photon energies, kinetic energies below 1500 eV can be achieved, which correspond approximately to 2 nm in probing depth for inorganic materials.

The possibility of acquiring photoemission spectra at higher kinetic energies, as high as 10 keV, has permitted the exploration of the chemical environment of sub-surface regions down to more than 20 nm for polymeric materials (Figure 6.1).[2]

Working with larger probing depths implies that surface contamination due to exposure to atmosphere is not as critical as compared to measurements performed with conventional XPS equipment. HAXPES reaches its full potential when using synchrotron radiation as excitation source since, in this case, photon energy and thus kinetic energy can be tuned, so that the probing depth can be also varied in a controlled and continuous manner. Nevertheless, the impinging beam can cause an irreversible damage on the surface and therefore, this is a drawback that has to be carefully addressed in any measurement, even for inorganic materials.[3,4]

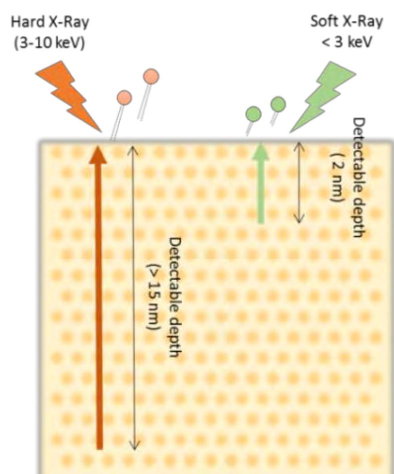

Figure 6.1. Schematic of XPS and HAXPES technique, showing the ability of HAXPES to measure deeper layers

In order to determine the main differences between the different methods developed to create chemical guiding patterns, the resulting surfaces have been characterized by using XPS and HAXPES. In this way, the interactions taking place between the surface and the BCP domains can be determined. Figure 6.2 shows a schematized description of the three approaches to create chemical guiding patterns developed at IMB-CNM, and previously described in *chapter 3*. The DSA processes that have been characterized are sustained on PS-OH brush layers.

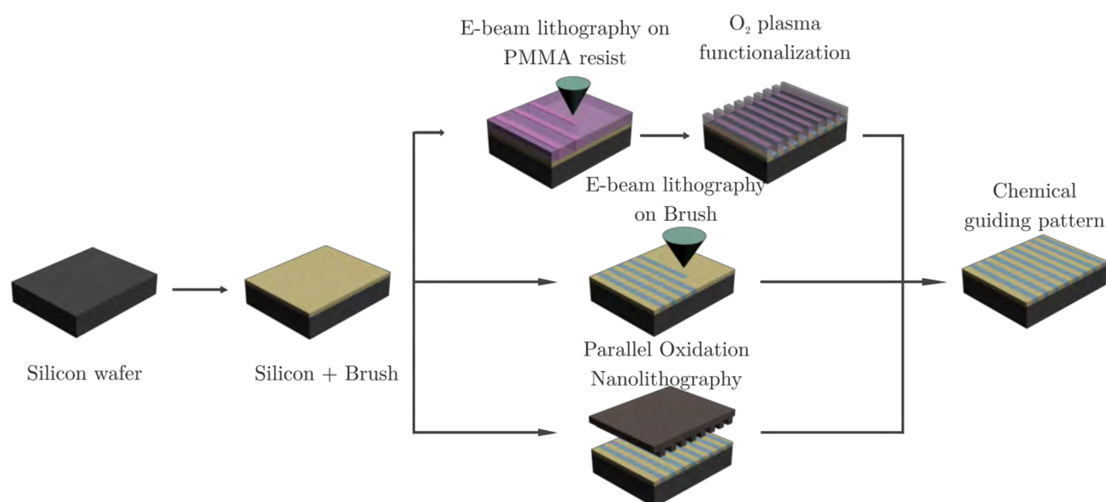

Figure 6.2. Schematized description of the three developed chemical epitaxy methods to DSA BCP. The method on top is the one based on using EBL on a resist and oxygen plasma to chemically functionalize the substrate, while in the other two nanolithography methods (middle and bottom) the guiding patterns are defined without using a resist (direct writing methods)

The HAXPES experiments have been performed at the HIKE end-station located at the KMC-1 beamline at the *BESSY II synchrotron of the Helmholtz Zentrum Berlin für Materialien und Energie* in Berlin (Germany).[5,6] Monochromatic radiation in the 2020-6000 eV photon energy range has been used for the experiments, impinging the sample surface at grazing incidence. Photoemitted electrons were collected with a *SCIENTA R4000* high-

resolution hemispherical analyzer at near normal emission, with an upper limit in kinetic energy of 10,000 eV. Experiments were performed in an ultrahigh vacuum chamber with a base pressure in the high 10^{-9} mbar range. To prevent beam damage, measurements were taken at different locations on the sample. In addition, the radiation was stopped when spectra were not acquired. On the other hand, ex-situ XPS experiments have been performed with a *SPECS PHOIBOS 150* hemispherical analyzer located at ICN2 using monochromatic AlKα radiation (1486.6 eV) as excitation source at a base pressure of 10^{-9} mbar.

As compared to the XPS system used, the HAXPES experiments have allowed getting higher energy resolution. Figure 6.3 shows the photoemission spectra of the Si2p line of the underlying silicon wafer taken with 2020 eV photons (lowest photon energy available). Both the signals arising from bulk Si (at 99.3 eV binding energy) and from SiO_2 (at around 104 eV binding energy) are displayed in the spectra. A least-square fit of the Si2p line after a Shirley-type background subtraction gives a spin-orbit splitting of 0.59 eV, the expected 2:1 branching ratio [$2p_{3/2}$:$2p_{1/2}$ with a nominal value of (2×3/2+1)/(2×1/2+1)] and a FWHM of 0.34 eV, highlighting the actual high resolution at use. Identical results are obtained for SiO_2/Si substrates, indicating the negligible effect of the brush on scattering of photoelectrons.

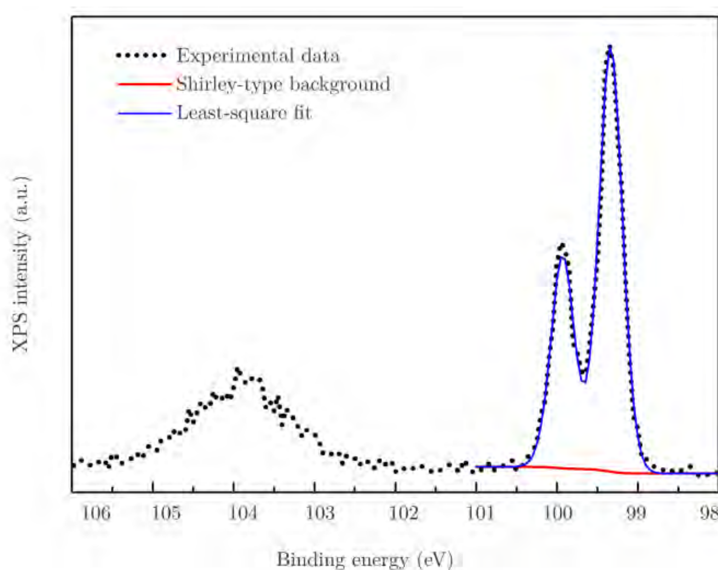

Figure 6.3. Photoemission spectra of the Si2p line taken with 2020 eV photons of a brush/SiO_2/Si sample. The discontinuous line stands for the experimental data while the continuous blue and red lines correspond to a least-square fit and to the chosen background, respectively

6.1.1. Characterization of chemical guiding patterns created by electron beam lithography and oxygen plasma functionalization

The approach based on using EBL and a subsequent oxygen plasma functionalization is the one depicted in section 3.2, and briefly described on the top of Figure 6.2. All the brush annealing processes have been performed within an oxygen free environment, since at the beginning of the research it was observed that the DSA processes did not work when the brush had been annealed in presence of oxygen. Therefore, in order to understand which is the origin of the DSA process efficiency, HAXPES experiments have been performed on un-modified PS-OH brush layers annealed under different conditions (cooled down in oxygen and nitrogen environment, respectively) and on the other hand, on functionalized surfaces.

Figure 6.4.a shows the experimental HAXPES C1s line (continuous black line) of the sample cooled down in nitrogen together with a least-square fit after background subtraction. The most prominent line (continuous red line), with a binding energy of 285.2 eV, corresponds to C-C and C-H sp^3-like bonding. The continuous blue line in Figure 6.4.a, with a binding energy of 286.5 eV, corresponds to the hydroxyl bonding of the PS-OH. The π-π^* shake-up feature at 291.8 eV, characteristic of a pure PS spectrum (continuous magenta line)[7], is also observed. Figure 6.4.b compares the zoomed in spectra of the C1s lines corresponding to the sample cooled in air (orange) and that cooled in nitrogen (black), respectively. The figure evidences a small but clear increase in intensity of the region corresponding to hydroxyl bonding for the sample cooled in air. We point out that this minor effect in the C1s line can only be observed because of the high-energy resolution used in the HAXPES experiments and that parallel XPS measurements of samples prepared under the same conditions did not show any significant difference. The higher density of hydroxyl bonding induces higher attraction to PMMA blocks due to the affinity with carbonyl PMMA groups. In this case, the chemical guiding patterns created afterwards on the sample cooled in air will not be effective since the brush is already slightly PMMA affine before the oxygen plasma functionalization. On the other hand, when the sample is cooled down in nitrogen, PS does not undergo oxidation. As a consequence, such sample is slightly affine to PS before functionalization. When chemical guiding stripes are defined on this substrate by oxygen plasma exposure (see Figure 6.5), there is enough chemical contrast to guide the alignment of the BCP. Therefore, it can be concluded that such a small increase in hydroxyl bonding is sufficient to disable the alignment capabilities of the PS-OH brush layer.

On the other hand, Figure 6.4.c shows the C1s HAXPES spectrum taken with 2020 eV photons of the sample cooled in nitrogen after the oxygen plasma treatment. The comparison with Figure 6.4.a evidences an increase in intensity towards higher binding energies in the ca. 286-291 eV region, which corresponds to contributions from different carbon-oxygen bonding configurations, as a result of the effect of the oxygen plasma

exposure on the PS-OH brush layer. The continuous blue line, corresponding to hydroxyl bonding, becomes more intense as compared to Figure 6.4.a Two new features are observed at 287.9 and 290 eV binding energies, which are assigned to the carbonyl (C-O, continuous green line) and carboxyl (O-C=O, continuous pink line) contributions, respectively. Thus, oxygen plasma activates the brush layer surface by creating a distribution of C-O bonding, while annealing and cooling in air induces essentially hydroxylation of the surface.

The combination between optimal processing conditions for grafting the polymer brush layer and an adequate chemical functionalization by oxygen plasma exposure leads to the possibility to generate efficient chemical patterns for guiding the self-assembly of the BCP.

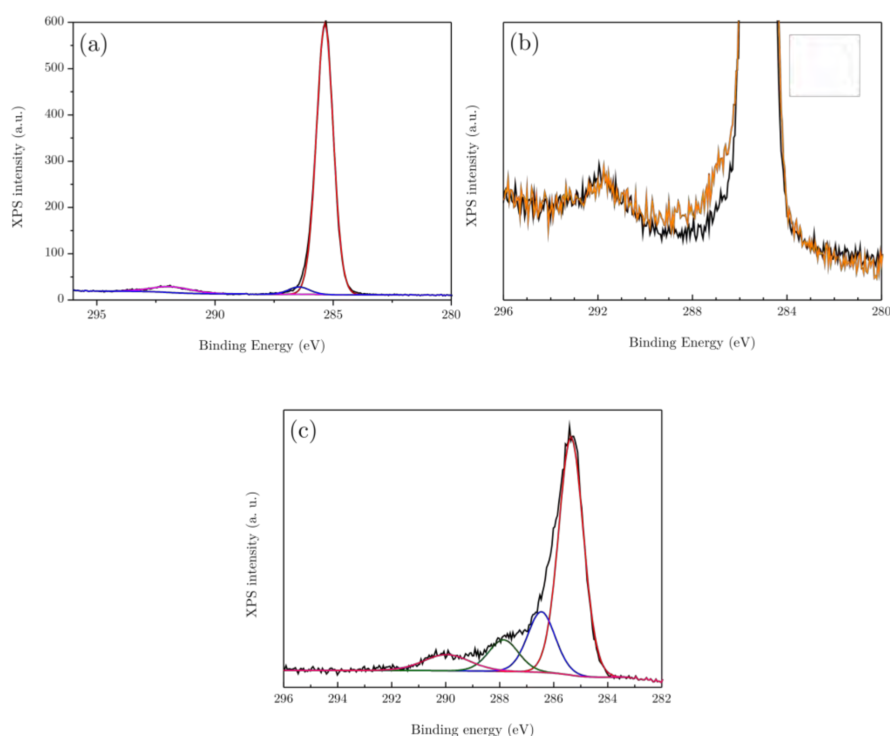

Figure 6.4. HAXPES spectra corresponding to the C1s region of grafted PS-OH samples (a) cooled in nitrogen, (b) cooled in air (orange) and in nitrogen (black) and (c) cooled in nitrogen and exposed to oxygen plasma taken with 2020 eV photon energy

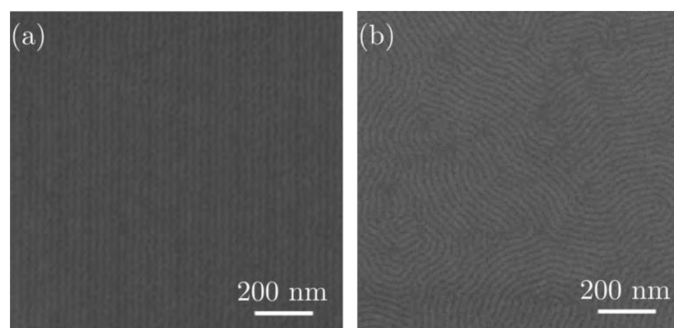

Figure 6.5. SEM images of PS-*b*-PMMA (L_0 = 28 nm) DSA for $4L_0$ density multiplication factor when using PS-OH brush layer annealed at (a) 230°C and cooled down in nitrogen and (b) 260°C and cooled down in air

Finally, the interfacial affinity between the PMMA block and both modified and un-modified brush layers has been studied by analyzing samples in which 20 nm PMMA films have been grown in top of modified and un-modified PS-OH.

Figure 6.6.a and b show the C1s HAXPES spectra acquired with 3000 eV photons together with de-convolutions using least-square fits. Both spectra show the characteristic 287.5 (continuous green line) and 290 eV (continuous magenta line) peaks of PMMA, corresponding to O-CH_3 and O-C=O configurations, respectively, with a 1:1 stoichiometric relationship.[8] The continuous red and blue lines correspond to C-C/C-H bonding and to hydroxyl bonding, respectively, as described in Figure 6.4. The intensity ratio between the C-C, C-H and C-OH contributions (red and blue lines) and the O-C=O contribution (magenta line) increases for the sample exposed to oxygen plasma as compared to un-exposed sample, indicating that for the latter the un-modified brush layer is not uniformly covered by relatively thick PMMA film, as a result of lower affinity between both materials (dewetting effect). However, in the case of the sample exposed to oxygen plasma the modified character of the brush layer triggers a higher affinity to PMMA (wetting).

This is further confirmed when the C1s HAXPES spectra are taken at different photon energies, as shown in Figure 6.6.c and d, where spectra have been acquired at 2700 and 3000 eV, respectively. In the case of the un-exposed sample the mentioned ratio increases strongly between both photon energies, as a result of the increasing contribution of the PS-OH substrate for increasing photon energy and thus of the probing depth, while for the exposed sample the ratio is almost constant indicating a uniformly covered substrate.

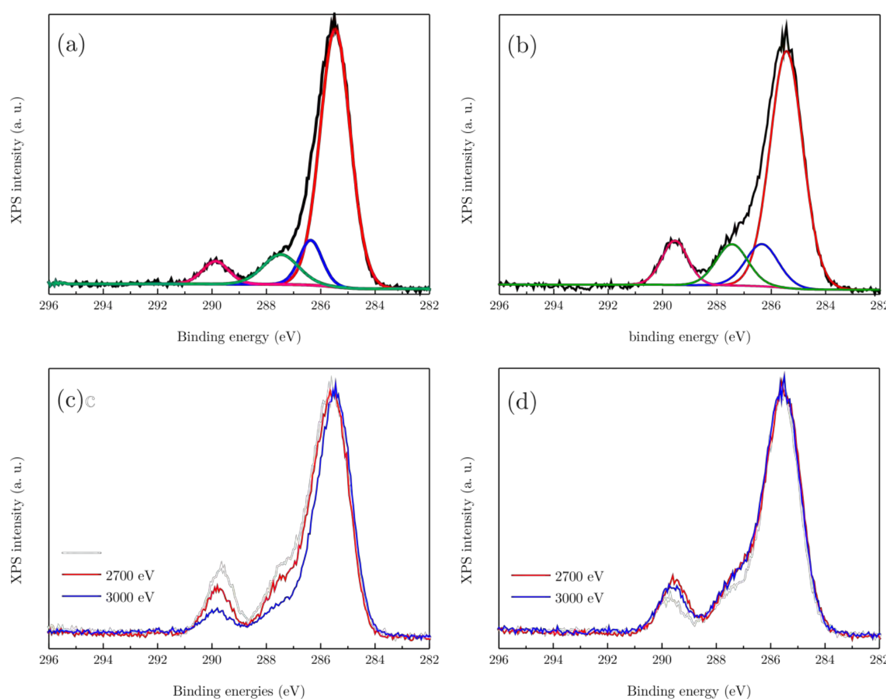

Figure 6.6. HAXPES spectra corresponding to C1s region of PMMA samples on (a) non-modified and (b) modified PS-OH taken with 3000 eV photons. (c) and (d) show a comparison with a lower photon energy (2700 eV)

6.1.2. Characterization of chemical guiding patterns created by direct writing techniques

These two chemical epitaxy approaches correspond to the two direct writing methods described in section 3.6, and schematized on the middle and bottom of Figure 6.2. The first method is based on using EBL to directly expose the sample to an electron beam which modifies the chemical affinity of the brush.[9] Rather, in the other approach the surface is locally oxidized by means of AFM.[10]

Due to the fact that the sample size needed for HAXPES characterization is larger than 0,5 µm, and taking into account that these are low speed writing techniques, both samples have been characterized in a Laboratory-Scale XPS Instrument where the modified areas on the sample are easier to locate. Nevertheless, in order to characterize the different interfaces on samples submitted to oxidation by SPL, the same process has been tried by Parallel Oxidation Nanolithography (PON)[11] which allows the oxidation of larger areas. This procedure has been performed in collaboration with the *Instituto de Ciencia de Materiales de Madrid* (ICMM), and it has been performed by contacting a conductive mold with the PS-OH surface while applying a voltage under conditions of high humidity (above 70%). The stamp consists of a 1 cm^2 piece of a DVD replica made with PDMS and coated with 100 nm thick gold film evaporated in high vacuum. The stamp's surface presents parallel hillocks 320 nm wide and spaced 740 nm. The height of the protrusions is 40 nm. To transfer the patterns from the stamp to the substrate, a 35 – 40 V bias voltage for a time ranging between 40 and 180 s has been applied while the stamps has been gently (50 kPa) pressed upon the substrate.

Figure 6.7.a shows a comparison between C1s XPS spectra of four PS-OH surfaces after annealing at 230°C and cooling down in nitrogen (continuous red line), after EBL and PON modification (continuous grey and blue line, respectively) and a freshly cleaved highly-oriented pyrolytic graphite (HOPG) surface (discontinuous black line). The surface modified by EBL shows a relatively large broadening and a strong shift towards lower binding energies, as compared to the sample modified by EBL and oxygen plasma (Figure 6.4.c). Charging effects can be excluded, since in all cases the energies have been referenced to the $Si2p_{3/2}$ peak (99.3 eV) from the buried silicon substrate. The mentioned shift towards lower binding energies denotes the increasing presence of sp^2 bonding based on the comparison with the results from a freshly cleaved HOPG sample (discontinuous black line), which shows a narrow peak centered at 284.4 eV characteristic of sp^2 bonding. Such increase in sp^2 bonding is in line, although not a direct proof, with the cross-linking of PS due to e-beam exposure, as has been reported in the literature[12–14], and which contributes to the alignment of the BCP, demonstrated in Figure 6.7.b.

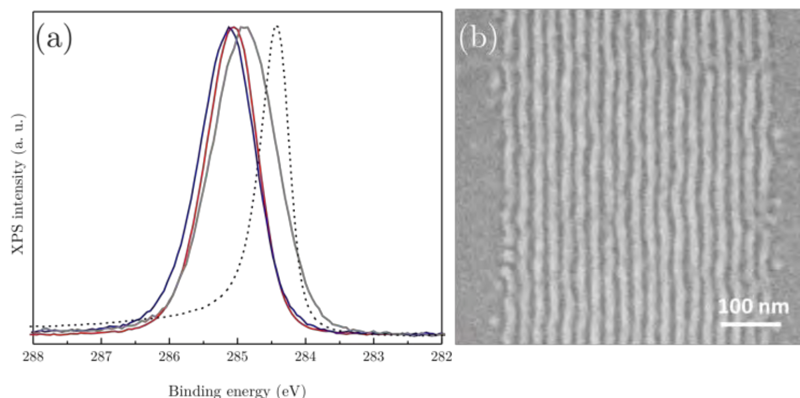

Figure 6.7. (a) C1s XPS spectra region of PS-OH (continuous red line), EBL and PON modified PS-OH (continuous grey and blue lines, respectively) and HOPG (discontinuous black line) using monochromatic 1486.6 eV photons and (b) SEM image of PS-*b*-PMMA DSA (L_0 = 22 nm) by EBL direct writing

On the other hand, Figure 6.8.a shows an AFM image of a chemical guiding pattern created by PON. The effect of the brush modification is an effective replication of the DVD pattern with modified regions (brighter in the AFM topography) slightly elevated (1.1 nm). Figure 6.8.b shows the Si1s spectra taken at different photon energies in the 2020-3000 eV range. At 2020 eV (black continuous line) only one feature is observed at about 1844 eV. At higher photon energies two more lines are identified at about 1841 and 1846 eV binding energies, respectively, that become increasingly dominant for increasing photon energies. The 1841 and 1846 eV features correspond to the buried Si/SiO_2 interface. Previous photoemission measurements performed at lower energy resolution using the Si2p line conclude that most of the oxide grown using PON is purely stoichiometric, although contribution from silicon lower oxidation states may be present.[14] In references[11,14,15] the Si2p spin-orbit splitting is not resolved (compare to Figure 6.3), which can preclude the observation of additional features in the region corresponding to the oxide.

In these experiments, Si1s line has been selected instead because of the higher interfacial sensitivity with photons above 2020 eV as compared to the Si2p line. At 2020 eV the corresponding kinetic energies are about 180 eV and 1920 eV for Si1s and Si2p, respectively, and the minimum mean free path for electrons in matter is at about 100 eV. Thus, we can continuously follow the emergence of the three features as a function of the increasing probing depth from the surface with the Si1s lines. In the case of the Si2p line photon energies above 200 eV should be used, which could not be achieved at the KMC-1 beamline. It can be concluded that the 1844 eV line emerges from a region located on top of the Si/SiO_2 interface, as schematized in Figure 6.8.a. In addition, since the feature at 1844 eV exhibits lower binding energy as compared to the 1846 eV counterpart, it is concluded that the 1844 eV line corresponds to a sub-stoichiometric oxide layer (SiO_x), with partially oxidized silicon. No changes are observed in the C1s spectra taken at the same photon energies, although they do not correspond to the same probing depths, since the associated kinetic energies are above 1735 eV for C1s.

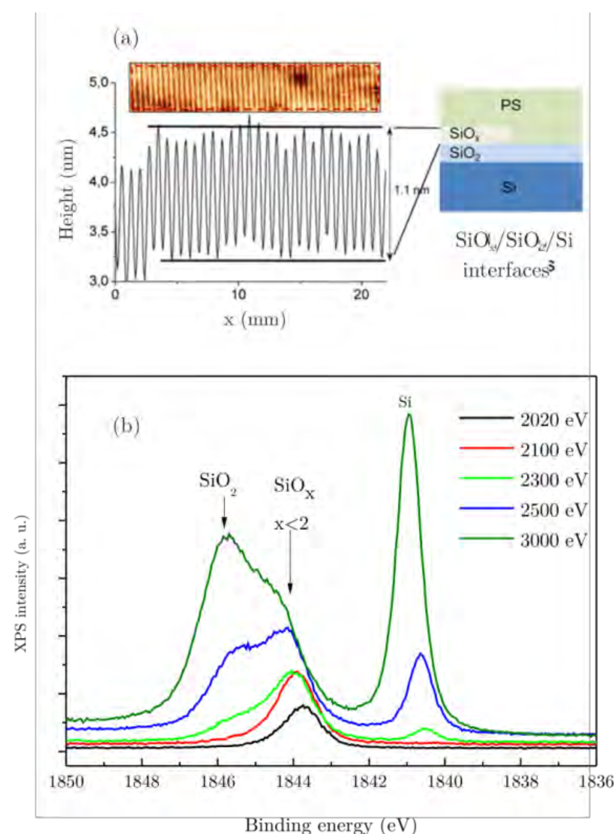

Figure 6.8. (a) AFM topography image and profile of the PS-OH brush surface after PON. A scheme is included showing the different regions and (b) HAXPES spectra of the Si 1s region at different incident energies

After characterizing these guiding patterns, it can be concluded that HAXPES using synchrotron radiation is a powerful spectroscopic tool to explore the chemical properties of surface and buried interfaces of brush layers for BCP DSA, since valuable information as a function of probing depth can be obtained.

Furthermore, it has been found that the choice of the accurate cooling down process after brush annealing is of paramount importance in order to obtain an optimal DSA result. HAXPES characterization shows an increase in intensity on the energy range corresponding to hydroxyl bonds when the brush is cooled down in the presence of oxygen. This is consistent with the change in the chemical affinity of the brush layer with the BCP experimentally observed in DSA.

With regard to the functionalization of the PS-OH brush layers, it has been proven that oxygen plasma exposure activates the brush layers by generating diverse carbon-oxygen bonding which promotes higher affinity to PMMA blocks while electron-beam exposure increases sp^2 bonding promoting higher affinity to PS blocks that might be explained by cross-linking of PS. In the case of parallel oxidation nanolithography, HAXPES provides experimental evidence of the existence of a sub-stoichiometric oxide between the brush layer and the SiO_2/Si substrate.

6.2. Block copolymer morphology and self-assembly characterization by GISAXS

GISAXS is a surface and sub-surface sensitive scattering technique which provides an accurate average structural information of as-received samples, with no need of sample manipulation.[16] In this method, the incident beam is almost totally reflected from the substrate followed by small-angle scattering of the refracted beam by the sample substrate.[17]

This technique allows the investigation of surfaces with thicknesses down to the sub-monomolecular range, providing information about the size and shape of nanostructures, as well as about their distribution. On the other hand, GISAXS experiments of polymeric thin films are limited to the use of synchrotron radiation since the scattering cross section is weak in the X-ray regime as compared with metals, because of the low atomic mass involved.[18,19]

The first examples in which GISAXS was used to characterize nanostructured films date from 1999, in which *Walter et al.* investigated the lateral structures of an ampholytic BCP, finding a good agreement with SPM measurements.[20] Since then, a large number of works analyzing the microphase separation in BCP have been reported[21–23], including those related with their use in microelectronics industry.[24] In this last example, *Ferrarese Lupi et al.* presented a work on high-aspect ratio PS-*b*-PMMA masks for lithographic applications.

The main advantages of GISAXS are that it is a non-destructive technique, and that the measurement is averaged on a large area. On the other hand, it can be used in different environment conditions (vacuum, air, gas atmospheres…). In addition, together with other parallel characterization techniques, it allows corroborating thin films structural information.

This is a technique which has to be used with synchrotron radiation and the obtained information has to be translated from the reciprocal to the real space. Furthermore, it is important to be aware of the radiation damage the sample can suffer, in order to avoid data which is contaminated by damage artifacts. On the other hand, due to the beam size, areas at the nanoscale are sometimes difficult to characterize.

6.2.1. Basis of grazing incidence X-ray technique

X-ray scattering of nanostructures shares the same principle as X-ray diffraction. In GISAXS, the incident X-ray vector is kept at a grazing angle and thus. Due to the small angles used, scattering comes from variations of the mean electronic density, which is simplified by basically considering variations in refractive index.

The geometry employed on the technique gathers the main particularity of GISAXS. Figure 6.9 shows a schematic representation of the GISAXS geometry. The incident X-ray beam of wave vector $\overrightarrow{k_i}$, impinges the surface with a very small incident angle, α_i, (close to the angle of total reflection, α_c) with respect to the sample surface. Then, the scattered intensity of wave vector $\overrightarrow{k_f}$, which makes a scattering angle of Ψ with respect to $\overrightarrow{k_i}$ and α_f with respect to the sample surface, is recorded with a two-dimensional (2D) detector. The sample-to-detector distances are normally between 2 and 5 m, and the values of the scattering vector, q, are in the range of 1 to 0.01 nm^{-1} (features from 1 to hundreds of nanometers can be evaluated by GISAXS).

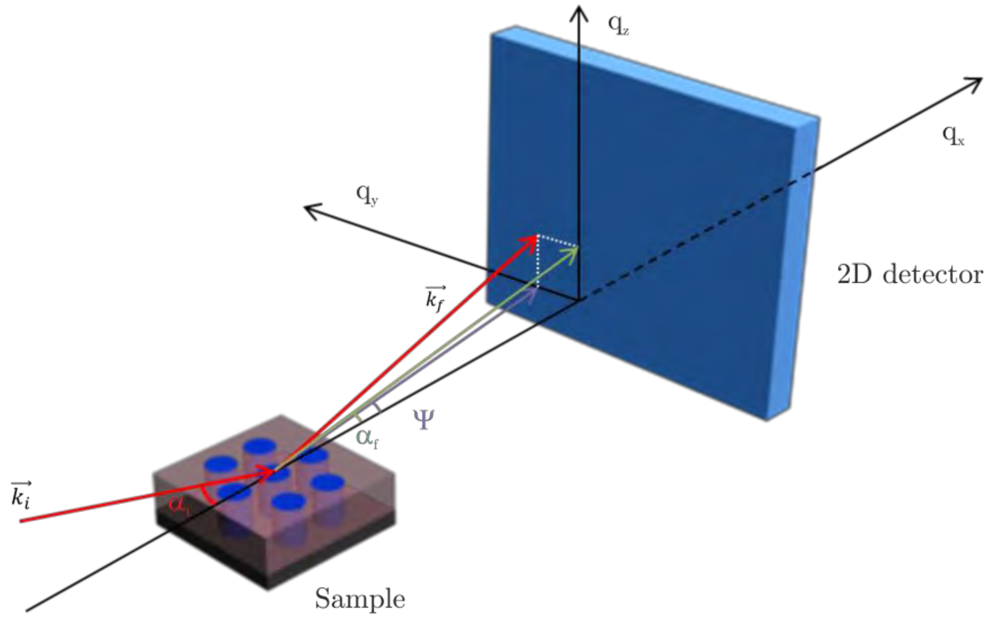

Figure 6.9. Schematic representation of GISAXS scattering geometry

The wave vector transfer, $\vec{q}$, is defined by the X-ray wavelength, λ, and related with the angular coordinates as described in equation (6.1):

$$\vec{q} = \overrightarrow{k_f} - \overrightarrow{k_i} = \frac{2\pi}{\lambda}\begin{pmatrix} \cos(\alpha_f)\cos(\psi) - \cos(\alpha_i) \\ \cos(\alpha_f)\sin(\psi) \\ \sin(\alpha_i)\sin(\alpha_f) \end{pmatrix}, \quad (6.1)$$

On the other hand, as previously mentioned, it is necessary to consider the effects of refraction at the surface since the incident angle, α_i, is very small.[25,26] Scattering originates from variation on the refractive index, which for X-ray is defined by equation (6.2).

$$n = 1 - \delta - i\beta, \quad (6.2)$$

where δ and β represent the dispersion and absorption contributions, respectively.

Arising at the critical angle, α_c, of the polymer there is a characteristic peak called *Yoneda Peak*[27], in which the diffuse scattering depends on the material and it is observed at the position $\alpha_i + \alpha_c$ relative to the direct beam on the detector.

$$\alpha_c = \sqrt{2\delta}, \tag{6.3}$$

There is another important peak called *specular peak* which satisfies the condition $\alpha_i = \alpha_f$. This peak can become very intense and therefore, in order to protect the detector against such high intensity, the detector has to be shielded with a beam stopper.

The X-ray penetration depth, Λ, is defined as the depth at which X-ray intensity is attenuated by 1/*e*. Therefore, by varying the incident angle, different structures through the film can be characterized. For α_i, α_c<1 and α_i=α_f, the equation results in (6.4):

$$\Lambda = \frac{\lambda}{4\pi}\sqrt{\frac{2}{\sqrt{\left(\alpha_i^2-\alpha_c^2\right)^2+4\beta^2}-\left(\alpha_i^2-\alpha_c^2\right)}}, \tag{6.4}$$

Once the data has been collected, the data has to be reduced by translating the detector pixels into reciprocal *q* space. Regarding the data reduction, there are different developed tools which mainly convert to *q* space and allow line cuts.

Concerning data analysis, as observed in equation (6.1), the intensity distribution in reciprocal space is built as a function of α_i, α_f, and 2θ. Therefore, the analysis of the reciprocal space is typically analyzed within the framework of kinematical approximations, such as the distorted-wave Born approximation (DWBA).[28,29] An analysis using DWBA results much more complex than the analysis of transmission data, but the basic concepts, form factor, *F(q)*, and structure factor, *S(q)*, are used as well.

6.2.2. Block copolymer self-assembly GISAXS characterization

The morphology of different BCP systems has been analyzed by GISAXS in order to get statistical information about the BCP size and spatial distribution.[30–32]

The experiments have been performed on the Austrian SAXS beamline at the *Elettra Sincrotrone Trieste* in Italy using a photon energy of 8.05 keV (λ=0.154 nm). The beam size at the sample position was 200 µm high and 1000 µm wide. Wide strips were used in front of the detector in order to stop the specular beam. All the GISAXS experiments have been performed at incident angles between 0.15° and 0.4° in order to have a wide exploratory analysis angle range.

On the other hand, the 0.15° angle was chosen because it is between the critical angle of the polymer film (0.12°) and that of silicon (0.163°). The scattered intensities have been

recorded with a *Pilatus 1M* detector (981 · 1043 pixels of 172 μm² size per pixel) mounted on the SAXS bench at a distance of 1877.824 mm from the sample.

6.2.3. Static GISAXS studies on block copolymer films

The analyzed samples are depicted in Table 6.1. PS-*b*-PMMA samples with different morphologies and molecular weights, as well as the high-χ systems studied in *chapter 5* have been characterized by GISAXS. All the samples have been prepared on 1 x 1 cm^2 chips bearing a native silicon oxide layer (p-type silicon wafers of 4-40 **Ω** · cm resistivity). Then, in order to obtain the BCP perpendicular morphology, the corresponding brush is spin-coated on the top of the substrate (see Table 6.1).

After having removed the non-reacted brush, the BCP is deposited and annealed to promote its self-assembly. SEM images showing the morphology of the different analyzed BCP samples, taken before GISAXS measurements, are shown in Figure 6.10.

Table 6.1. BCP samples characterized by GISAXS

Sample	Brush	Specifications
PS-*b*-PMMA	$PS_{60\%}$-*r*-PMMA	Lamellar
		Lamellar
		Lamellar
	$PS_{70\%}$-*r*-PMMA	Cylindrical
PS-*b*-PLA	$PS_{48\%}$-*r*-PMMA	Lamellar
PLA-*b*-PDMS-*b*-PLA	$PS_{60\%}$-*r*-PMMA + PDMS-OH	Lamellar

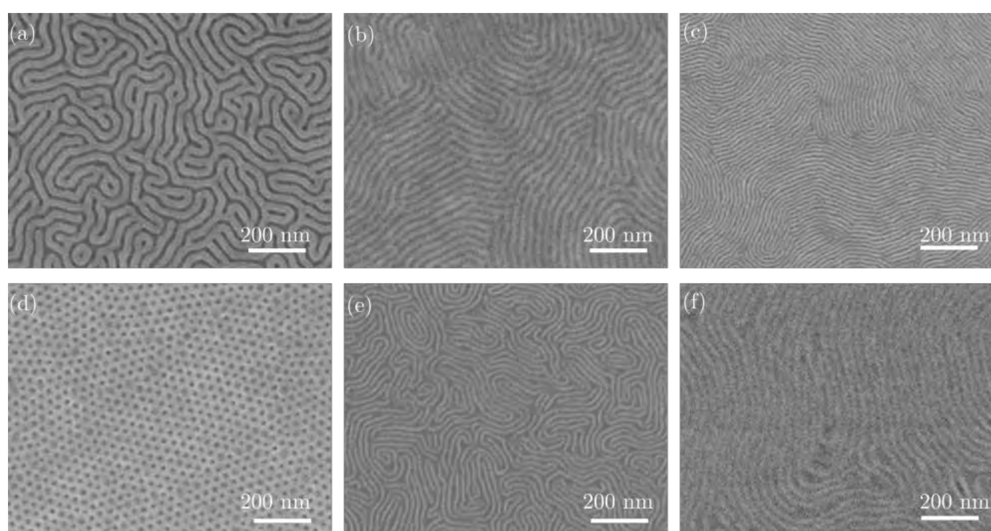

Figure 6.10. SEM images of lamellar PS-*b*-PMMA with (a) L_0=38 nm, (b) L_0=28 nm, (c) L_0=22 nm, (d) cylindrical PS-*b*-PMMA with L_0=35 nm, (e) lamellar PS-*b*-PLA, and (f) lamellar PLA-*b*-PDMS-*b*-PLA

GISAXS patterns are obtained by following the procedure depicted in Figure 6.11. The image represents the GISAXS detector pixels *x* and *y,* in the corresponding axis. Then, the

patterns are obtained by making an horizontal cut of 30 pixels thick in 267 pixel, and translating it into the *q* space. This pixel corresponds to an angle $\alpha_f = 0.193°$ and $q_z = 0.03$ nm^{-1}.

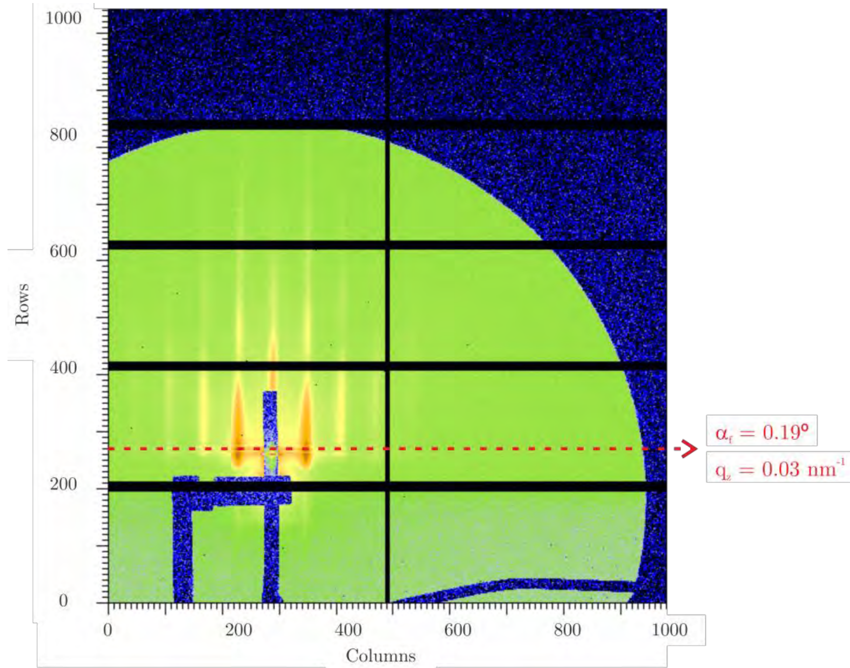

Figure 6.11. Scheme of a GISAXS pattern showing all GISAXS sectors. The cuts are performed in the sector in which the center of the reflected beam is located

Figure 6.12 shows the SEM images of the lamellar (L_0 = 38 nm) and cylindrical PS-*b*-PMMA, and the corresponding GISAXS patterns. Since GISAXS transforms structural parameters in real space into the reciprocal space, the vertical rods are directly related with the d-spacing of the BCP.

For a lamellar and cylindrical BCP, it is related by equations (6.5) and (6.6), respectively.

$$L_0 = \frac{2\pi}{q}, \tag{6.5}$$

$$L_0 = \frac{4\pi}{\sqrt{3}q}, \tag{6.6}$$

For lamellar (L_0 = 38 nm) and cylindrical BCPs, vertical rods (10 Brag rod) are equally spaced at an interval of Δq = 0166 and 0.203 nm^{-1}, respectively. The corresponding real-space period is thus, 38.27 and 36.01 nm, respectively, which is in agreement with previous SEM measurements.

The L_0 measurements for the other BCP systems, as well as a comparison with the pitch measurement extracted from SEM, are depicted in Table 6.2. The difference between the SEM and GISAXS measurements for the cylindrical BCP is attributed to the change of the PS matrix under the high electron beam inducing its cross-linking.[33]

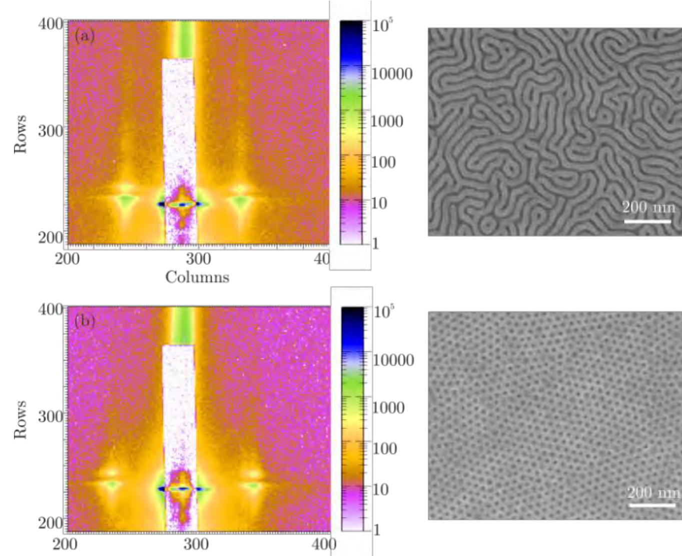

Figure 6.12. GISAXS patterns and SEM images of (a) lamellar and (b) cylindrical PS-*b*-PMMA samples before removing PMMA

Table 6.2. BCP samples characterized by GISAXS

Sample	SEM pitch	GISAXS Pitch	GISAXS Pitch after PMMA etching
PS-*b*-PMMA	38 nm	38.27 nm	38.70 nm
	28 nm	28.06 nm	28.06 nm
	22.5 nm	23.07 nm	23.06 nm
	35 nm	36.01 nm	36.01 nm
PS-*b*-PLA	19.5 nm	19.09 nm	-
PLA-*b*-PDMS-*b*-PLA	30 nm	29.52 nm	-

On the other hand, in order to have more contrast and get information in the film volume, these samples have been compared with those in which the PMMA domains have been previously removed by exposing the samples to a brief dose of oxygen plasma. Figure 6.13 and Figure 6.14 show the GISAXS patterns and their intensity profiles along the 10 Bragg rod, for the lamellar and cylindrical PS-*b*-PMMA. From the GISAXS patterns of Figure 6.13 it can be seen that there is higher electronic density contrast between PS and PMMA, as compared with the ones in Figure 6.12, due to the PMMA removal. This allows not only the measurement of the 10 Bragg rod, but also of higher order rods.

On the one hand, it is observed that the 10 Bragg position stays unchanged after the PMMA removal (see Table 6.2). On the other, in contrast with Figure 6.14.a, Figure 6.14.b shows the characteristic positions of the 2D hexagonal arrays, representative from the perpendicular oriented cylindrical phase. These peaks are indexed as the *(h,k)* reflections of a two-dimensional hexagonal lattice (equation (6.7)), and the results obtained are in well agreement with the ones reported in the literature.[34,35]

$$q = \frac{4\pi\sqrt{h^2+hk+k^2}}{\sqrt{3}L_0}, \qquad (6.7)$$

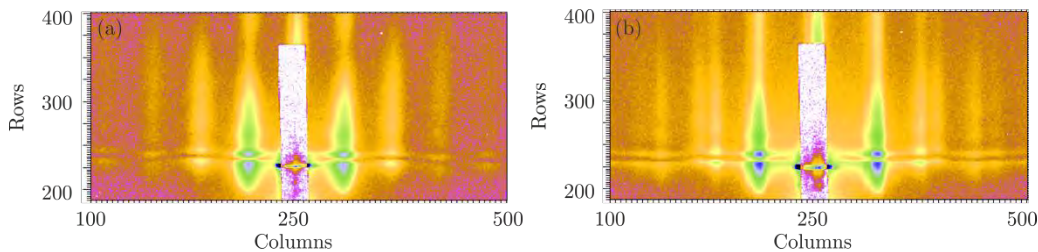

Figure 6.13. GISAXS patterns of (a) lamellar and (b) cylindrical PS-*b*-PMMA samples after removing PMMA by oxygen plasma exposure

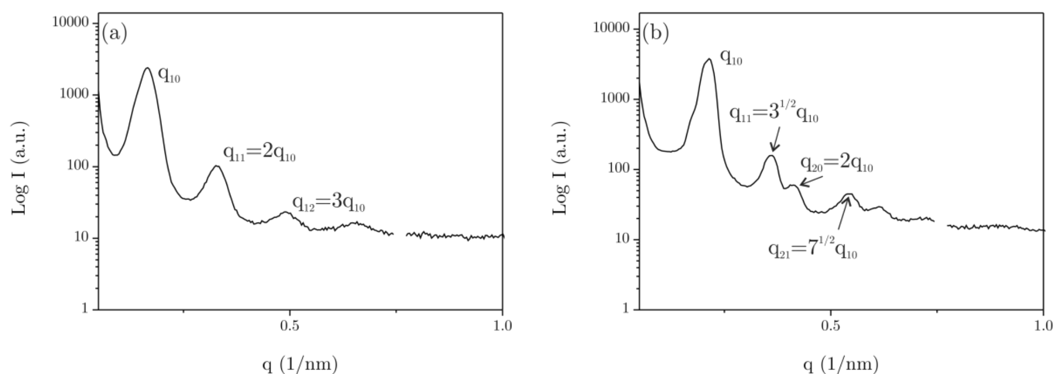

Figure 6.14. GISAXS intensity profile along the 10 Bragg rod for (a) lamellar (L_0 = 38 nm) and (b) cylindrical PS-*b*-PMMA

Regarding the high-χ samples, the same analysis procedure described above has been followed. Figure 6.15 shows the GISAXS intensity profiles for PS-*b*-PLA and PLA-*b*-PDMS-*b*-PLA samples. As it is observed, there is enough contrast between the domains to see a sharp primary peak in both cases. Furthermore, for the PLA-*b*-PDMS-*b*-PLA sample the appearance of a higher order rod is observed (Figure 6.15.b).

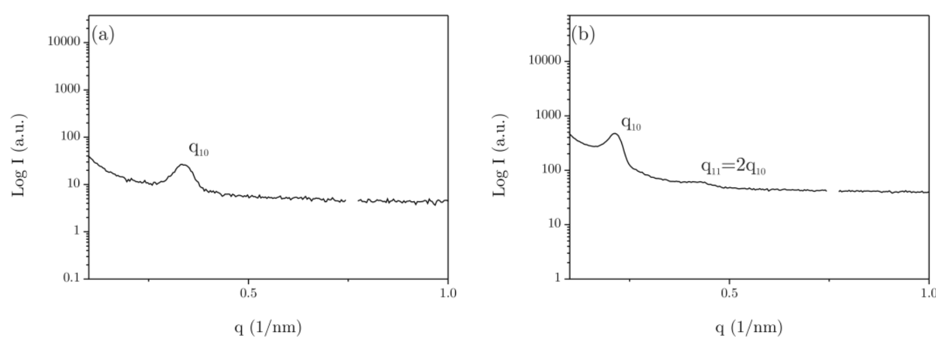

Figure 6.15. GISAXS intensity profile along the 10 Bragg rod for lamellar high-χ (a) PS-*b*-PLA and (b) PLA-*b*-PDMS-*b*-PLA

6.3. Summary and conclusions

In summary, two different techniques to further characterize BCP films and their interactions with the substrate have been presented.

With regard to guiding pattern characterization, it has been demonstrated that HAXPES using synchrotron radiation is a powerful technique to explore the chemical properties of surface and buried interfaces in the DSA process.

The different interactions which take place on the chemically modified guided patterns have been characterized. On the one hand, when the brush is functionalized by using exposure under oxygen, the plasma activates the brush by generating diverse C-O bonding promoting higher affinity to PMMA blocks. On the other hand, when the polymer surface is exposed to direct electron beam exposure, it cross-links as reflected in the increase of sp^2 bonding. In the case of parallel oxidation nanolithography, HAXPES provides experimental evidence of the existence of a sub-stoichiometric oxide between the brush layer and the SiO_2/Si substrate.

Concerning the analysis of BCP films, GISAXS measurements have allowed a well-defined structure characterization of lamellar and cylindrical BCPs. Furthermore, it has been demonstrated the different profiles between lamellar and cylindrical perpendicular oriented BCPs, by selectively removing one of the domains.

6.4. References

1. Edited by Wolfgang Drube. Recent advances in Hard X-ray Photoelectron Spectroscopy (HAXPES). *J. Electron Spectros. Relat. Phenomena* **190,** 125–314 (2013).

2. Felicissimo, M. P. *et al.* Determination of vertical phase separation in a polyfluorene copolymer: fullerene derivative solar cell blend by X-ray photoelectron spectroscopy. *J. Mater. Chem.* **19,** 4899–4901 (2009).

3. Subías, G., *et al.* Characterization of the anion-ordering transition in (TMTTF) 2 ReO4 by x-ray absorption and photoemission spectroscopies. *Phys. Rev. B - Condens. Matter Mater. Phys.* **76,** 1–7 (2007).

4. Fraxedas, J. *et al.* Modulation of surface charge transfer through competing long-range repulsive versus short-range attractive interactions. *J. Phys. Chem. C* **115,** 18640–18648 (2011).

5. Schaefers, F., *et al.* KMC-1: A high resolution and high flux soft x-ray beamline at BESSY. *Rev. Sci. Instrum.* **78,** 1–14 (2007).

6. Gorgoi, M. *et al.* The high kinetic energy photoelectron spectroscopy facility at BESSY progress and first results. *Nucl. Instruments Methods Phys. Res. Sect. A Accel. Spectrometers, Detect. Assoc. Equip.* **601,** 48–53 (2009).

7. Way, W. K., *et al.* Polystyrene by XPS. *Surf. Sci. Spectra* **2,** 67 (1993).

8. Rosencrance, S. W., *et al.* Polymethylmethacrylate by XPS. *Surf. Sci. Spectra* **2,** 71–75 (1993).

9. Evangelio, L. *et al.* Creation of guiding patterns for directed self-assembly of block copolymers by resistless direct e-beam exposure. *J. Micro/Nanolith. MEMS MOEMS.* **14,** 33511 (2015).

10. Fernández-Regúlez, M., Evangelio, L., *et al.* F. Sub-10 nm Resistless Nanolithography for Directed Self-Assembly of Block Copolymers. *ACS Appl. Mater. Interfaces* **6,** 21596–21602 (2014).

11. Albonetti, C. *et al.* Parallel-local anodic oxidation of silicon surfaces by soft stamps. *Nanotechnology* **19,** 435303 (2008).

12. Varlot, K., Martin, J. M. *et al.* Physical and chemical changes in polystyrene during electron irradiation using EELS in the TEM: Contribution of the dielectric function. *J. Microsc.* **191,** 187–194 (1998).

13. Massey, S., *et al.* Chemical Modification of Polystyrene by Low-Energy (<100 eV) Electron Irradiation Studied by Mass Spectrometry. *J. Appl. Polym. Sci.* **108,** 3163–3168 (2008).

14. Klauser, R. *et al.* Oxidation states in scanning-probe-induced Si[sub 3]N[sub 4] to SiO[sub x] conversion studied by scanning photoemission microscopy. *Appl. Phys. Lett.* **79,** 3143 (2001).

15. Lazzarino, M. *et al.* Atomic force microscope anodic oxidation studied by spectroscopic microscopy. *Appl. Phys. Lett.* **81,** 2842 (2002).

16. Smilgies, D. M., *et al.* Characterization of Polymer Thin Films with Small-Angle X-ray Scattering under Grazing Incidence (GISAXS). *Synchrotron Radiat. News* **15,** (2002).

17. Levine, J. R., *et al.* Grazing-incidence small-angle X-ray scattering: new tool for studying thin film growth. *J. Appl. Crystallogr.* **22,** 528–532 (1989).

18. Müller-Buschbaum, P. *et al.* Determination of micrometer length scales with an X-ray reflection ultra small-angle scattering set-up. *EPL (Europhysics Lett.* **42,** 517 (1998).

19. Smilgies, D. M., *et al.* Characterization of Polymer Thin Films with Small-Angle X-ray Scattering under Grazing Incidence (GISAXS). *Synchrotron Radiat. News* **15,** (2002).

20. Walter, H. *et al.* Lateral structures of thin films of ampholytic diblock copolymers absorbed from dilute aquieous solution at the solid/liquid interface. *Langmuir* **15,** 6984–6990 (1999).

21. Daillant, J., *et al.* Grazing incidence surface scattering of X-rays. *J. Chem. Soc.{,} Faraday Trans.* **92,** 505–513 (1996).

22. Müller-Buschbaum, P. *et al.* Correlated Roughness, Long-Range Correlations, and Dewetting of Thin Polymer Films. *Macromolecules* **31,** 3686–3692 (1998).

23. Xu, T. *et al.* Scattering Study on the Selective Solvent Swelling Induced Surface Reconstruction. *Macromolecules* **37,** 2972–2977 (2004).

24. Ferrarese Lupi, F. *et al.* High Aspect Ratio PS-b-PMMA Block Copolymer Masks for Lithographic Applications. *ACS Appl. Mater. Interfaces* **6,** 21389–21396 (2014).

25. Jackson, J. D. *Classical Electrodynamics*. (John Wiley and Sons, 1999).

26. Peng, Q., *et al.* Nanoscopic patterned materials with tunable dimensions via atomic layer deposition on block copolymers. *Adv. Mater.* **22,** 5129–5133 (2010).

27. Yoneda, Y. Anomalous Surface Reflection of X Rays. *Phys. Rev.* **131,** 2010–2013 (1963).

28. Sinha, S. K., *et al.* X-ray and neutron scattering from rough surfaces. *Phys. Rev. B* **38,** 2297–2311 (1988).

29. Baumbach, G. T., *et al.* The influence of specular interface reflection on grazing incidence X-ray diffraction and diffuse scattering from superlattices. *Phys. B Condens. Matter* **198,** 249–252 (1994).

30. Smilgies, D., *et al.* Characterization of polymer thin films with small-angle X-ray scattering under grazing incidence (GISAXS). *Synchrotron Radiat. News* **15,** 35–42 (2002).

31. Busch, P., *et al.* Structure of Thin Films of Lamellar Poly(styrene-b-butadiene) Diblock Copolymers As Revealed by Grazing-Incidence Small-Angle Scattering. *Macromolecules* **40,** 630–640 (2007).

32. Hexemer, A. *et al.* Advanced grazing-incidence techniques for modern soft-matter materials analysis. *IUCrJ* **2,** 106–125 (2015).

33. Freychet, G. *et al.* Removal of poly(methyl methacrylate) in diblock copolymers films studied by grazing incidence small-angle X-ray scattering. *J. Polym. Sci. Part B Polym. Phys.* **54,** 1137–1144 (2016).

34. Ferrarese Lupi, F. *et al.* High Aspect Ratio PS-b-PMMA Block Copolymer Masks for Lithographic Applications. *ACS Appl. Mater. Interfaces* **6,** 21389–21396 (2014).

35. Fleury, G. *et al.* Development and integration of systems with enhanced resolutions based on Si-containing block copolymers for line space applications. **9425,** 94250Z (2015).

Chapter 7

Pattern transfer of block copolymers and application in device fabrication

The nanoscale BCP mask features formed on the substrate after self-assembly present very poor contrast etching and are easily damaged after plasma processing. Therefore, an accurate pattern transfer method is required.
This chapter introduces a method based on the use of atomic layer deposition (ALD) to enhance the etching contrast between PS and PMMA, and thus perform the pattern transfer of the features into the substrate. It has been characterized by Peak Force tapping AFM which has made possible to access the local mechanical properties of single BCP domains.
On the other hand, the application of BCP DSA in microelectronics is presented, with the fabrication of a novel nanomechanical resonator made by graphoepitaxy and infiltrated material by ALD.

7.1. Conventional atomic layer deposition

7.1.1. Introduction

Atomic layer deposition (ALD) is a vapor phase deposition technique which can produce thin, highly uniform and conformal films of a variety of materials. It is based on sequential, self-limiting and surface controlled vapor phase reactions capable of achieving a control on the film growth at the nanometer or sub-nanometer scale.[1,2] The film formation mechanism consists of consecutive atomic layers grown from the surface at relatively low temperatures.

The number of ALD applications has been significantly increased over the past few years, especially due to the constantly decrease of the IC device size. ALD is a very suitable method for the fabrication of nanostructures with high aspect ratio, because it offers functional material layers with high quality, uniformity and conformality.[3] On the other hand, ALD has been also used for biomedical applications, for the creation of biomedical coatings, and for optical sensors.[4]

In contrast to chemical vapor deposition (CVD), the precursors are not injected simultaneously in the reactor; they are instead inserted as a series of sequential pulses. In each pulse, the precursor reacts with the surface until the reaction is completed. Therefore, the amount of material deposited on a surface depends on the interactions between the precursor and the surface.[5]

The ALD surface reaction mechanisms are depicted in Figure 7.1, and as observed, it consists on the sequential use of self-terminating gas-solid reactions. The following 4-steps are involved: (i) the first precursor (A, red) is introduced in the chamber, and it reacts with the reactive sites of the surface until they are consumed, (ii) the remaining reactant molecules and the secondary reaction products are evacuated, (iii) the second precursor (B, green) is inserted into the reactor, and after the reaction (iv) the chamber is purged. This mechanism represents one ALD cycle, and in each reaction cycle a certain amount of material to the surface is added, until the desired thickness is achieved.

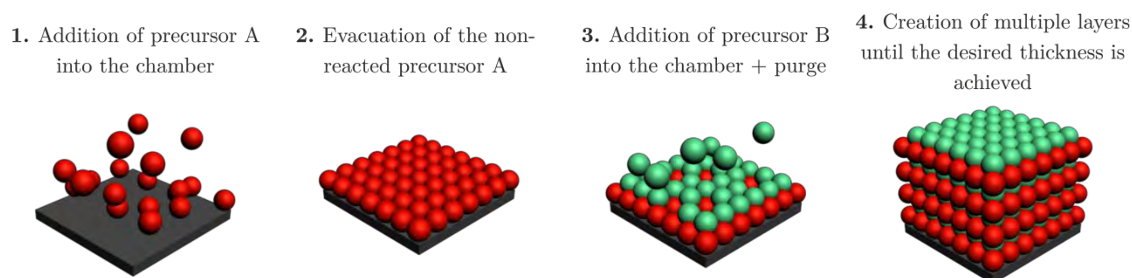

Figure 7.1. ALD surface reaction mechanism

ALD processes have been developed for a wide range of inorganic materials, like oxides, nitrides, sulphides, selenides and others.[5] However, among all the processes published in the literature, the synthesis of Al_2O_3 from trimethylaluminum (TMA) and water is the mostly known. The reactants are very reactive and thermally stable, which means that the self-limited growth of alumina can be achieved in a wide range of temperatures.[5]

The reaction mechanism sequence is described in Figure 7.2. First the TMA precursor chemisorbs on the substrate reacting with the adsorbed hydroxyl groups, until the surface is passivated (TMA does not react with itself, thus the reaction leads to one layer). Next, the non-reacted precursor and the secondary products (CH_4) are pumped out of the chamber, normally by using argon or nitrogen as purge gases, leaving a surface covered with $AlCH_3$ groups (reaction (7.2)). Afterwards, the water vapor is pulsed into the chamber and reacts with the methyl groups of the surface forming Al-O bridges and hydroxyl surface groups. Finally, the chamber is purged with argon or nitrogen, and the secondary products are pumped away (reaction (7.3)). The overall stoichiometry reaction is (7.1), and it is often described by two half-reactions (7.2) and (7.3).

$$Al(CH_3)_{3(g)} + 3/2\ H_2O_{(g)} \rightarrow 1/2\ Al_2O_{3(s)} + 3CH_{4(g)}, \tag{7.1}$$

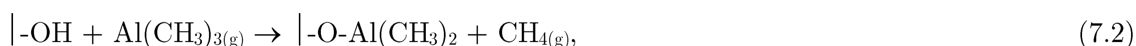

$$|\text{-OH} + Al(CH_3)_{3(g)} \rightarrow |\text{-O-}Al(CH_3)_2 + CH_{4(g)}, \tag{7.2}$$

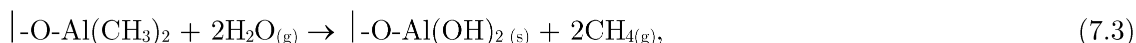

$$|\text{-O-}Al(CH_3)_2 + 2H_2O_{(g)} \rightarrow |\text{-O-}Al(OH)_{2\ (s)} + 2CH_{4(g)}, \tag{7.3}$$

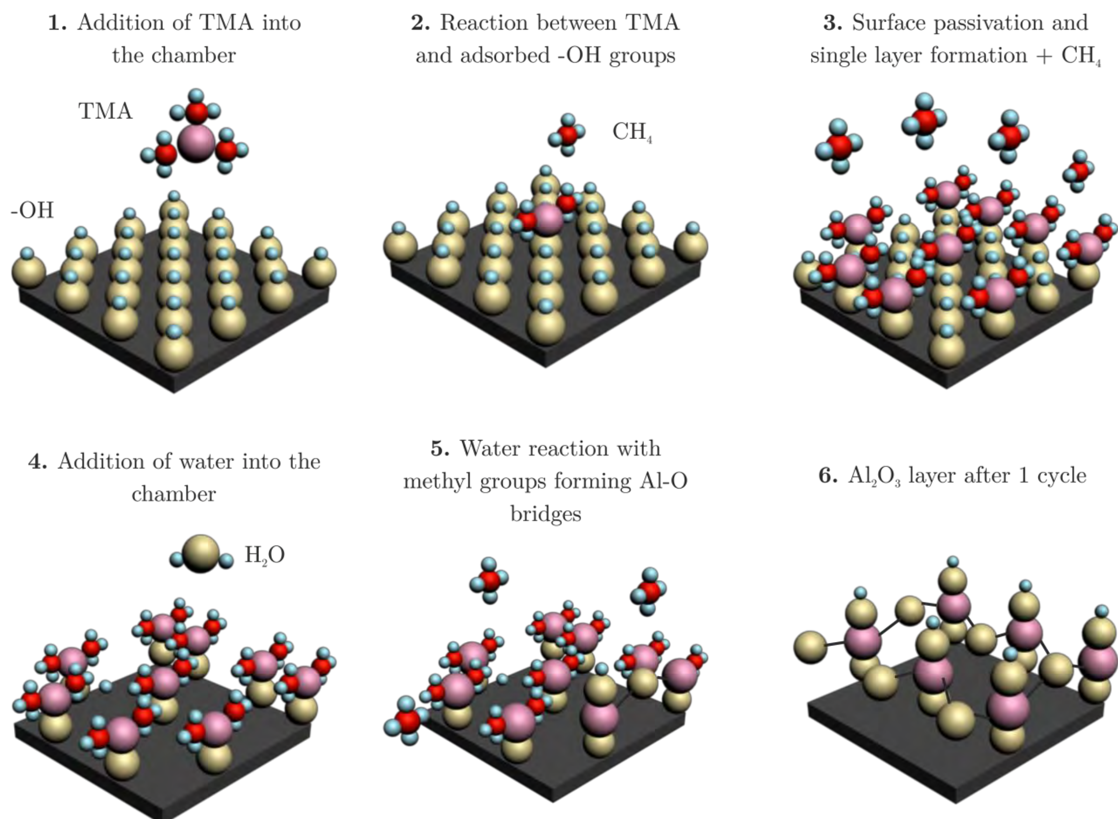

Figure 7.2. Al_2O_3 reaction mechanism sequence

When ALD is used with polymer surfaces, it has been demonstrated that precursors can infiltrate and react to modify significantly their mechanical properties.[6] In particular, PMMA presents a characteristic bonding structure (hydroxyl and carbonyl) which allows the ALD film nucleation and growth. A possible mechanism for the reaction between TMA and PMMA is presented in Figure 7.3. The PMMA carbonyl groups react with the TMA molecules forming an acetal group by transferring the methyl to the carbon. Then, the water, reforms the carbonyl not in the ester form but in the ketone form.

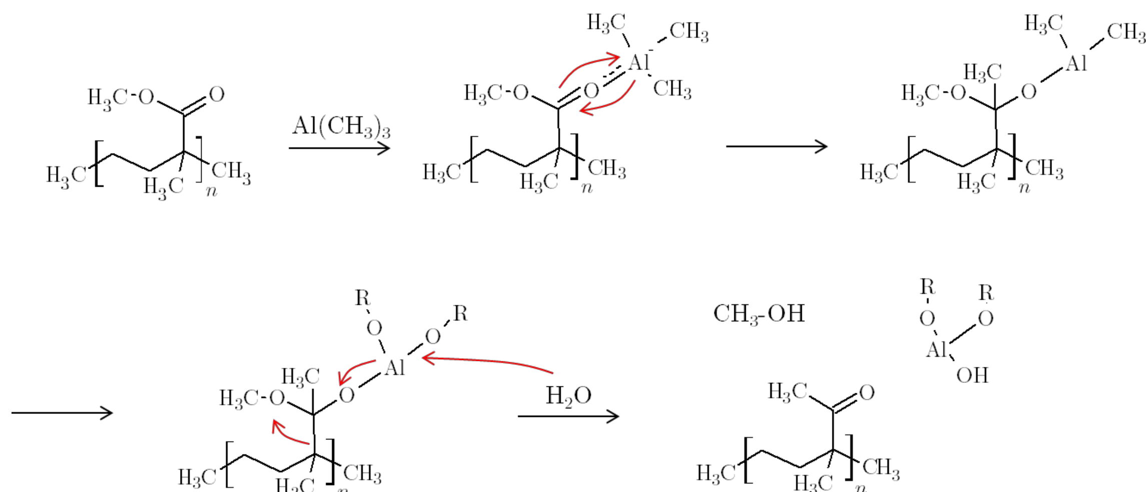

Figure 7.3. Possible mechanism for the reaction between TMA (Lewis acid) and PMMA carbonyl groups (Lewis base), followed by the reaction with water (R denotes PMMA)[6]

The ability of controlling the reactions between the precursors and polymers, is being used on the field of BCP DSA, to enhance the etching BCP properties, by selectively depositing the material in only one of the domains.[6,7]

7.1.2. Use of atomic layer deposition for block copolymer pattern transfer

To take advantage of the nanostructures offered by BCP DSA, accurate pattern transfer techniques are needed. Normally, to enhance the etch resistance of the BCP film to oxygen plasma, the pattern is transferred to an intermediate hard mask layer.[8,9] However, in order to avoid the complication on the fabrication process and the associated additional costs, selective deposition by means of ALD is used.[10–12]

The ALD technique provides a powerful nanofabrication technique for BCP DSA pattern transfer, since it enhances the etching contrast between BCP domains, and thus allows obtaining high-aspect ratio nanostructures. ALD organometallic precursors exhibit higher chemical affinity to one of the domains, thus allowing the selective deposition on one of the blocks. The etching contrast between domains is enhanced because for each cycle, there is a selective deposition by ALD, which produces a selective growth of material on top of the preferential domain.

The use of ALD has been performed with TMA precursor and water, to selectively grow Al_2O_3 on top of PMMA domains of a PS-*b*-PMMA BCP. As discussed in the previous section, it has been reported that Al_2O_3 is selectively deposited on PS-*b*-PMMA BCP samples, due to the preferential chemical interactions between the TMA molecules and the carbonyl moieties along the PMMA chains.[11–14]

7.1.2.1. Materials and methods

The ALD process has been performed on self-assembled PS-*b*-PMMA samples, as depicted in Figure 7.4. The whole process consists of 5-steps: (i) PS-*b*-PMMA self-assembly, (ii) selective alumina deposition on PMMA domains, (iii) PS removal, (iv) silicon etching and (vi) ALD mask removal.

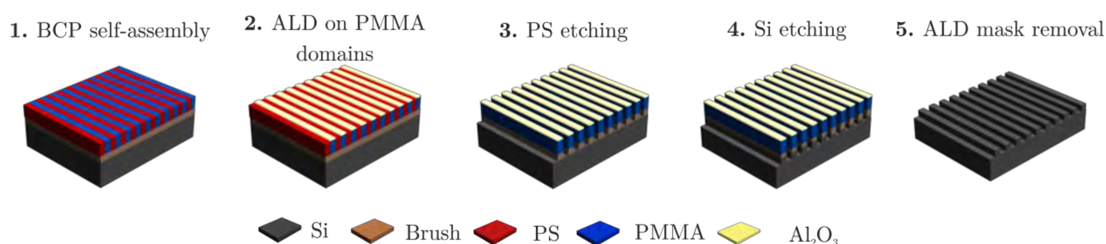

Figure 7.4. Schematic of ALD on PMMA domains of PS-*b*-PMMA sample

After the PS-*b*-PMMA (L_0 = 28 nm) BCP is self-assembled, Al_2O_3 is selectively deposited on top of PMMA domains by using five ALD cycles. The ALD process has been performed in a *Savannah* equipment from *Cambridge Nanotech*.

The alumina is synthesized using binary reactions of TMA (*Aldrich*, 97%) and water within the polymer films. The deposition is performed at 85°C as follows: first, the chamber is stabilized with nitrogen for 10 min. Then, the precursor, TMA, is admitted into the reactor for 60 s. Afterwards, the chamber is purged with nitrogen for further 60 s, and the water is admitted in the reactor for 60 s. Finally, this sequence is repeated for five cycles.

7.1.2.2. PS-b-PMMA pattern transfer results

After PS-*b*-PMMA self-assembly, the alumina is deposited on top of the material for five cycles, and the obtained results are shown in Figure 7.5.

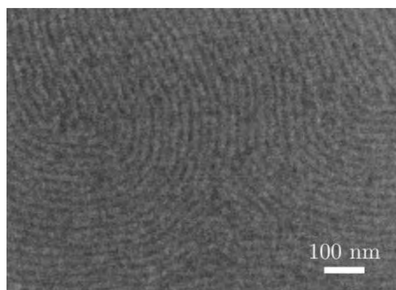

Figure 7.5. SEM image of PS-*b*-PMMA self-assembly after five cycles of ALD deposition

After selectively depositing the alumina on PMMA domains, an oxygen plasma exposure at 300W and 50 sccm of oxygen flow is performed to remove the PS domains (Step 3 of Figure 7.4). The PS etching has been studied for different times, and the obtained results are shown in Figure 7.6. As observed, the higher the etching time, the more damaged the BCP structure is. From the SEM images it is observed that the optimal etching time is 5 s. Nevertheless, the hard mask used to transfer into the silicon would not withstand the etching, since it is easily damaged when exposing to slightly higher times of oxygen plasma.

This occurs because the alumina is only deposited on the top of PMMA domains, but it is not infiltrated through the whole domain. Therefore, when exposing the sample to oxygen plasma, the PS domains start to be removed because the PMMA is protected by the alumina (step 2 of Figure 7.7). Afterwards, as the PMMA domains are not protected by the alumina in the edges but only on the top, they also start to be etched. Consequently, as the PMMA etching speed is faster than for PS, the whole PMMA domains (now not protected by the alumina) are removed (step 3 of Figure 7.7), and only a thin PS layer remains on the surface (step 4 of Figure 7.7).

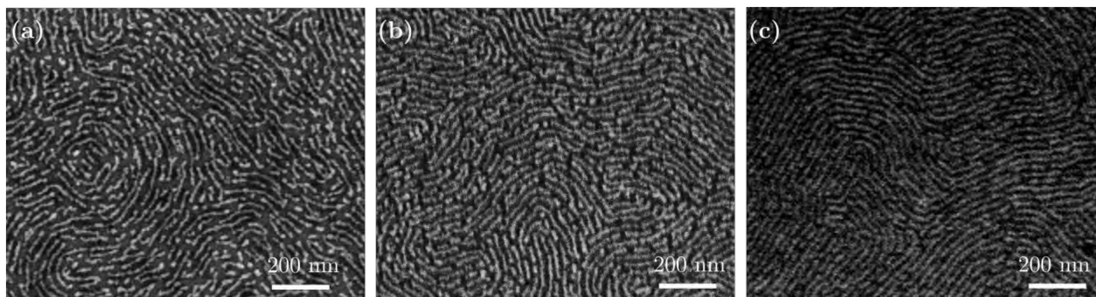

Figure 7.6. SEM image of PS-*b*-PMMA self-assembly after three cycles of ALD deposition and oxygen palsma exposure for (a) 60 s, (b) 30 s and (c) 5 s etching times

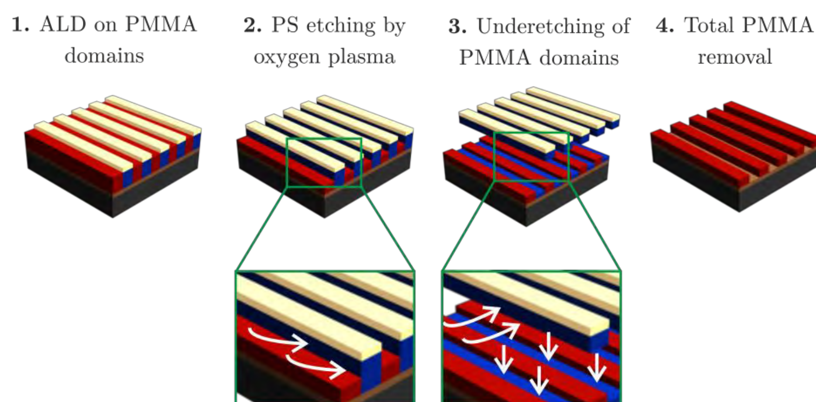

Figure 7.7. Schematic representation of the PS etching process during oxygen plasma exposure

7.2. Sequential Infiltration Synthesis

7.2.1. Introduction

SIS offers an alternative ALD mechanism which allows the infiltration of the precursors into the polymer.[7,10–12,15,16] On the BCP field, it is used to selectively infiltrate one BCP domain, and use this protective component as a hard mask to pattern transfer.

Moreover, the thermal budget of SIS is low and it shares the same conventional ALD reaction mechanism. However, whereas ALD implies surface reactions, SIS uses functional moieties within the bulk of the polymer. As a consequence, when samples are exposed to SIS conditions, not only the polymer top domains are covered but the whole polymer domains are infiltrated, resulting in an improvement of resist hardness.

7.2.2. Use of sequential infiltration synthesis for pattern transfer

As observed in the previous section, the conventional ALD mechanism does not protect the whole PMMA domains and therefore, it cannot act as a hard mask for pattern transfer since it is under-etched after some seconds of oxygen plasma exposure. As an alternative solution SIS, which has been demonstrated to lead to high-aspect-ration features in a substrate, is used.[7,11,12,16–18]

It has been reported that the mechanism which takes place during the reaction between TMA and PMMA in the SIS process involves two-step reaction.[12] In the first step (7.4), TMA reacts with the carbonyl groups of PMMA and form a physisorbed complex ($C{=}O \cdot\cdot\cdot Al(CH_3)_3$), which slowly reacts to form a permanent O-Al bond (7.5).

$$C{=}O + Al(CH_3)_3 \leftrightarrow C{=}O \cdot\cdot\cdot Al(CH_3)_3, \tag{7.4}$$

$$C{=}O \cdot\cdot\cdot Al(CH_3)_3 \rightarrow O\text{-}Al\text{-}(CH_3)_2, \tag{7.5}$$

It has been found out that TMA purge times are crucial for the infiltration process, since longer purge times reduces the SIS growth. On the other hand, longer TMA exposure times, enhance the alumina formation, since the intermediate complex concentration is maintained, and it allows the slow reaction of the chemisorbed species.[11,12]

7.2.2.1. Materials and methods

The overall process describing the SIS mechanism is shown in Figure 7.8. As observed, it has the same processing steps as the one described for the conventional ALD deposition (Figure 7.4).

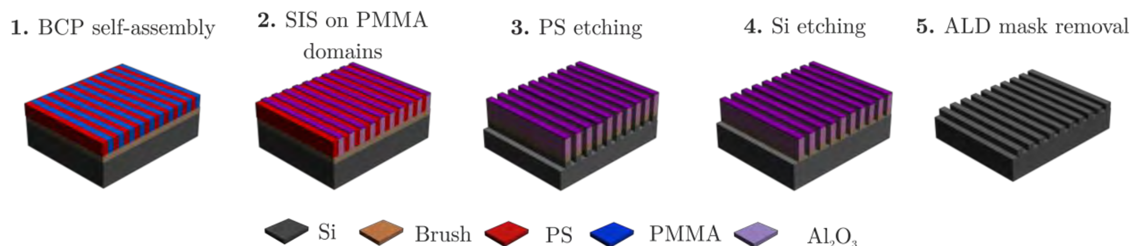

Figure 7.8. Schematic of SIS on PMMA domains of PS-*b*-PMMA sample

After PS-*b*-PMMA self-assembly, the SIS is performed in the same ALD equipment, but by varying the processing conditions in order to induce the diffusion of the alumina into the PMMA domains.

The infiltration is performed at 85°C as follows: first, the chamber is purged and the TMA is admitted at a P=0.5 torr for 80 s. Then, the non-reacted gases are evacuated with nitrogen for 30 s, and the water is introduced into the chamber for further 80 s. Finally, the chamber is purged for 30 s. This sequence is then repeated for several cycles.

The main differences between conventional ALD and SIS, are the pressure reached inside the chamber after the precursor admission, the time the precursor is inside the chamber, and the purge time. It has been reported that in order to obtain an optimal SIS process, it is recommended to work at higher pressures and larger purge times.[10,16]

7.2.2.2. PS-b-PMMA pattern transfer results

After trying the optimal SIS conditions on a self-assembled PS-*b*-PMMA sample, it was found that the optimal number of cycles when using these conditions was 5. Figure 7.9 shows PS-*b*-PMMA self-assembly SEM images before and after SIS, for a lamellar (L_0 = 38 nm) and a cylindrical (L_0 =35 nm) BCP.

As observed in the images, the infiltration is performed on the PMMA domains, as better revealed on the cylindrical SEM images. The cylindrical BCP has a PS/PMMA composition of 60:40, so that the BCP morphology consists of PMMA cylinders immersed in a PS matrix. In Figure 7.9.b it is observed that the cylinders (PMMA domains) exhibit higher contrast compared with Figure 7.9.a, due to the alumina infiltration.

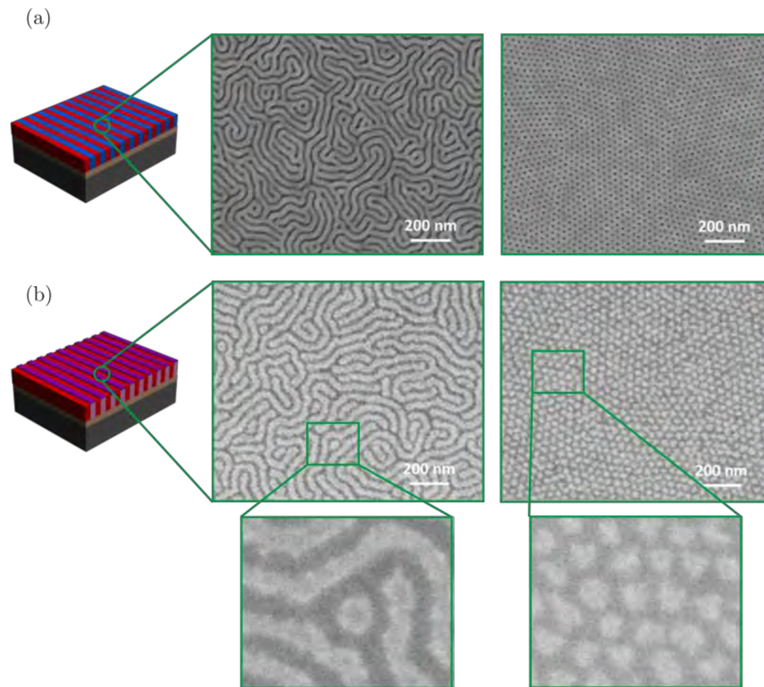

Figure 7.9. SEM images of lamellar (L_0 =38 nm) and cylindrical (L_0 =35 nm) BCP (a) before and (b) after 5 cycles of SIS

In order to explore the degree of infiltration in the PMMA domains, the samples have been exposed to oxygen plasma at 300W with a 50 sccm oxygen flow, for 18 s to etch the PS block. Afterwards, it has been performed a silicon etching by using the conditions depicted on Table 7.1 for 60 s to etch 15 nm silicon.

Table 7.1. Silicon etching conditions for PS-*b*-PMMA pattern transfer

[SF_6]	20 sccm
[C_4F_8]	30 sccm
Power Source	220 W
Chuck Power	20 W
Time	60 s
Pressure	2 Pa
Temperature	20°C
Silicon etched	15 nm

Figure 7.10 and Figure 7.11 show top-view and cross-section SEM images, respectively, of the PS-*b*-PMMA silicon pattern transfer, after being removed the infiltrated PMMA hard mask. As observed from the images, the features have been successfully transferred to the substrate, thus demonstrating the viability of the method to obtain high-aspect ratio nanostructures. There has been performed an EDX characterization, and the presence of alumina has not been detected. However, since the alumina mask is hard to remove by oxygen plasma, a thin alumina layer can remain on top of etched silicon.

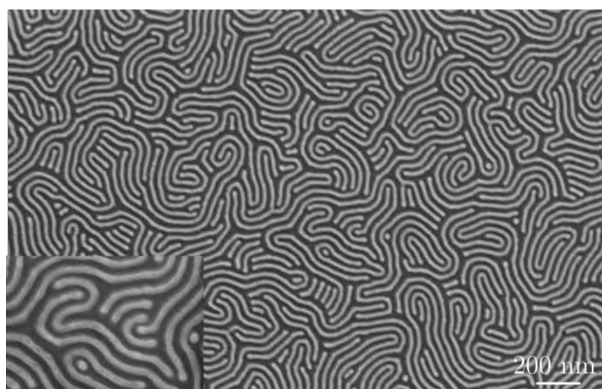

Figure 7.10. SEM image of lamellar (L_0 =38 nm) BCP after pattern transfer the features into the silicon by using an infiltrated PMMA mask

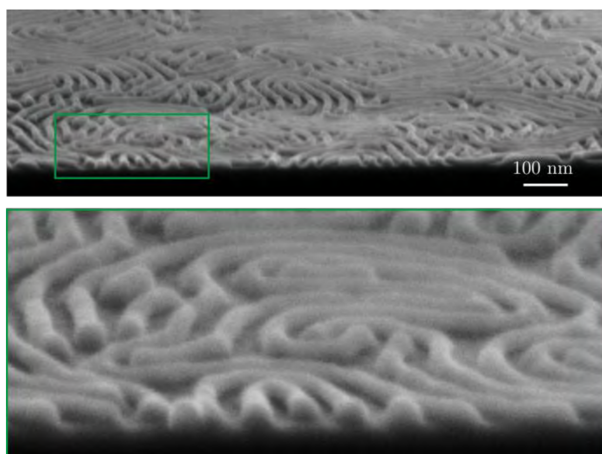

Figure 7.11. Cross-section SEM image of lamellar (L_0 =38 nm) BCP after pattern transfer the features into the silicon by using an infiltrated PMMA mask. The lower image corresponds to the zoomed part region (green) of the image above

7.2.2.3. High-χ block copolymers pattern transfer results

In order to demonstrate the applicability of the SIS process to other material systems, the procedure depicted in Figure 7.8 has been tried on two high-χ systems: PS-*b*-PLA and poly(1,1-dimethyl silacyclo-butane)-*b*-poly(methyl methacrylate) (PDMSB-*b*-PMMA).

PDMSB-*b*-PMMA samples have been provided by LCPO, and it consists of a cylindrical BCP where PMMA cylinders are immersed in a PDMSB matrix. Figure 7.12 shows the PDMSB-*b*-PMMA self-assembly after SIS and PS etching, and it is observed that after the process the PMMA cylinders have been infiltrated as the ones for PS-*b*-PMMA in Figure 7.9.b.

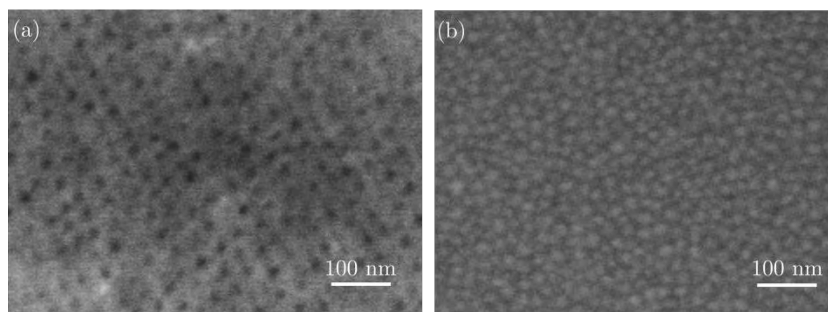

Figure 7.12. SEM images of PDMSB-*b*-PMMA self-assembly (a) before and (b) after SIS and PS etching

On the other hand, the SIS process has been used for PS-*b*-PLA, where the selective infiltration takes place with the PLA block in a similar mechanism as the PMMA does, due to the carbonyl groups present on the PLA molecular structure. As observed in Figure 7.13.b, after an oxygen plasma etching, the PS domains are etched away, and the PLA infiltrated mask resists, allowing thus a subsequent pattern transfer. On the other hand, the morphology the BCP takes when it is dissolved in PGMEA, reveals that the wider domains are the ones infiltrated corresponding to the PLA, as previously discussed in *chapter 5*.

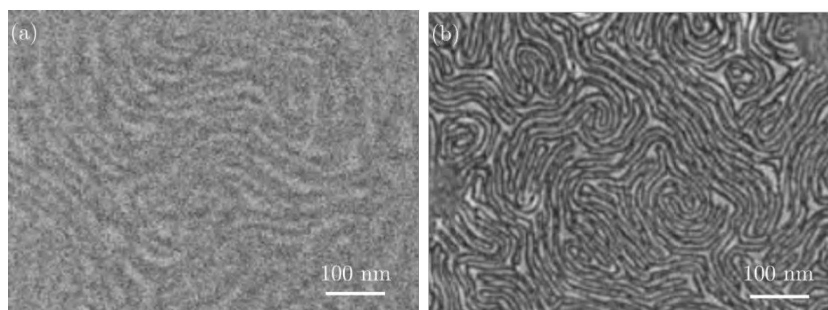

Figure 7.13. SEM images of PS-*b*-PLA self-assembly (a) before and (b) after SIS and PS etching

7.3. Local nanomechanical properties of PS-*b*-PMMA self-assembly

7.3.1. Introduction

In order to characterize the enhancement on the mechanical properties when the BCP films are covered and infiltrated with alumina, the *Peak Force* quantitative nanomechanical mapping (QNM) technique was used.

With this technique, it is possible to reliably quantify the Young's modulus, *E*, of materials with high spatial resolution and surface sensitivity. This is achieved by the acquisition of a large number of force-distance curves to calculate the mechanical properties at each point.[19]

When probing ultrathin films, the film thickness is in the order of magnitude of the indentation performed. Therefore, the tip also feels the substrate and as a consequence, the mechanical properties are dominated by the substrate, resulting in a larger apparent

modulus compared to the bulk ones.[20] To avoid this effect, it is widely accepted to limit the indentation depth to less than 10% of the film thickness.[21,22]

Figure 7.14 shows a force-separation curve obtained with a single approach (blue) and withdraw (red) on a PS reference sample. The deformation parameter is obtained from a portion of the approach curve (blue). In order to determine the Young's modulus from the curve, the curve is fitted to the Derjaguin-Muller-Toporov (DMT) model (modified Hertzian model that also takes adhesive forces into account)[23], which provides the reduced modulus, E^*, as a function of the applied force, the maximum adhesion, F_{adh}, force and the instantaneous sample deformation, d_{sample} (equation (7.6)).

$$F = \frac{4}{3}E^*\sqrt{Rd_{sample}^3} + F_{adh}, \quad (7.6)$$

where the relation between the reduced modulus and the sample modulus is approximately $E = 0.88E^*$, if it is assumed that the tip modulus is larger than the sample modulus (when using silicon-based tips with polymer surfaces).

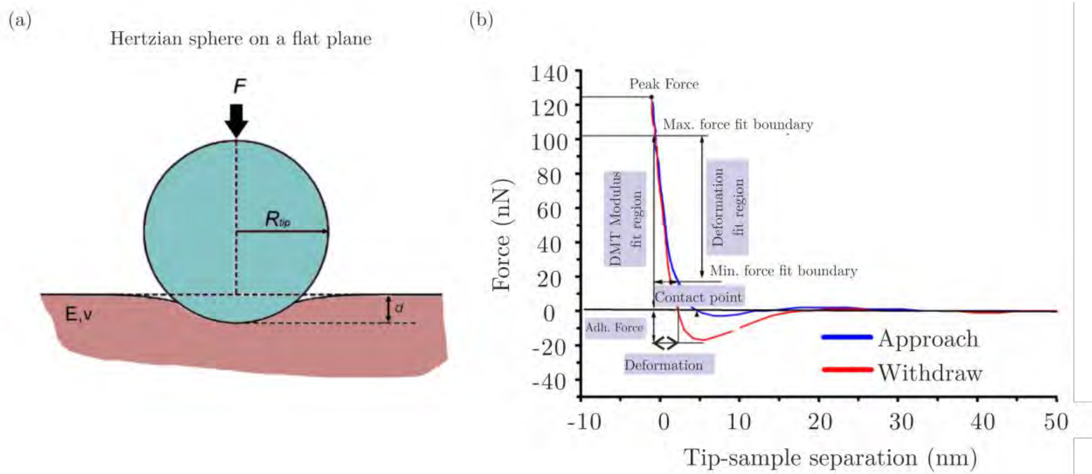

Figure 7.14. (a) Hertz contact model for a spherical indenter and (b) typical force plot of a PS reference sample of E = 2.7 GPa obtained with a cantilever of k = 42 N/m

Finally, the tip radius values have been obtained by using a calibration kit from *PELCO*.[24] The tip radius is calculated from the height profile when scanning a mica substrate with attached Au spherical nanoparticles with a nominal radius of 5 nm.

7.3.2. Optimal Indentation Conditions

The surface imaging has been obtained by using an AFM (*Dimension Icon, Bruker*) operating in Peak Force tapping mode, by using standard tapping cantilevers with a nominal radius of 7 nm and with a nominal spring constant of 26 N/m.

By calibrating the optical lever sensitivity, cantilever spring constant and tip radius, the force-distance curve can be obtained with information about the Young's modulus, adhesion force, sample deformation and dissipated energy.

In order to obtain a detectable deformation, the correct cantilever spring constant has to be selected. For sample Young's modulus in the 1 GPa to 10 GPa range, force constants in the order of about 25 N/m are indicated. In the experiments, the applied force set points have been in the range between 10 and 25 nN, to get an optimal deformation for a reliable fit (1-2 nm) avoiding plastic deformation.[14]

Figure 7.15.b shows the Young's modulus map for a PS film (E = 2.7 GPa) at various Peak Force set points to identify the optimal indentation conditions. From the force-distance graph (Figure 7.15.c) it is observed that when the deformation reaches 2.1 nm, the value of the modulus does not change with respect to the force applied, matching the nominal value of the reference.

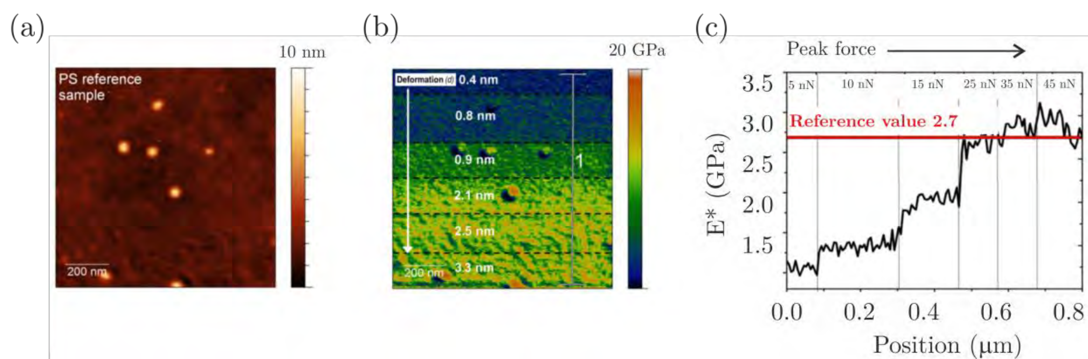

Figure 7.15. (a) AFM topography image and (b) reduced modulus of a PS reference film. The value of the sample reduced modulus, E^*, is plotted along the position in (c)

7.3.3. Characterization of PS-*b*-PMMA thin films

Once the deformation range has been obtained, a PS-*b*-PMMA thin film of 38 nm pitch has been characterized after self-assembly. Its specifications are depicted in Table 7.2.

Table 7.2. Specifications of PS-*b*-PMMA

Sample	M_n	Morphology	Thickness	E^*_{PS}	E^*_{PMMA}
PS-*b*-PMMA	79 kg/mol	Lamellar	43 nm	1.97 ± 0.21 GPa	3.10 ± 0.73 GPa

The experiments have been performed by keeping constant the deformation between 1 and 4 nm and with a standard silicon tip. AFM topography, adhesion, modulus and deformation channels are presented in Figure 7.16.b-e. From the images, it is observed that PS is softer and deforms more resulting in a higher adhesion. The value of E^* reported in Table 7.2, is obtained by fitting the modulus distribution to two Gaussians, each one representing the modulus distribution of each phase (Figure 7.16.j).

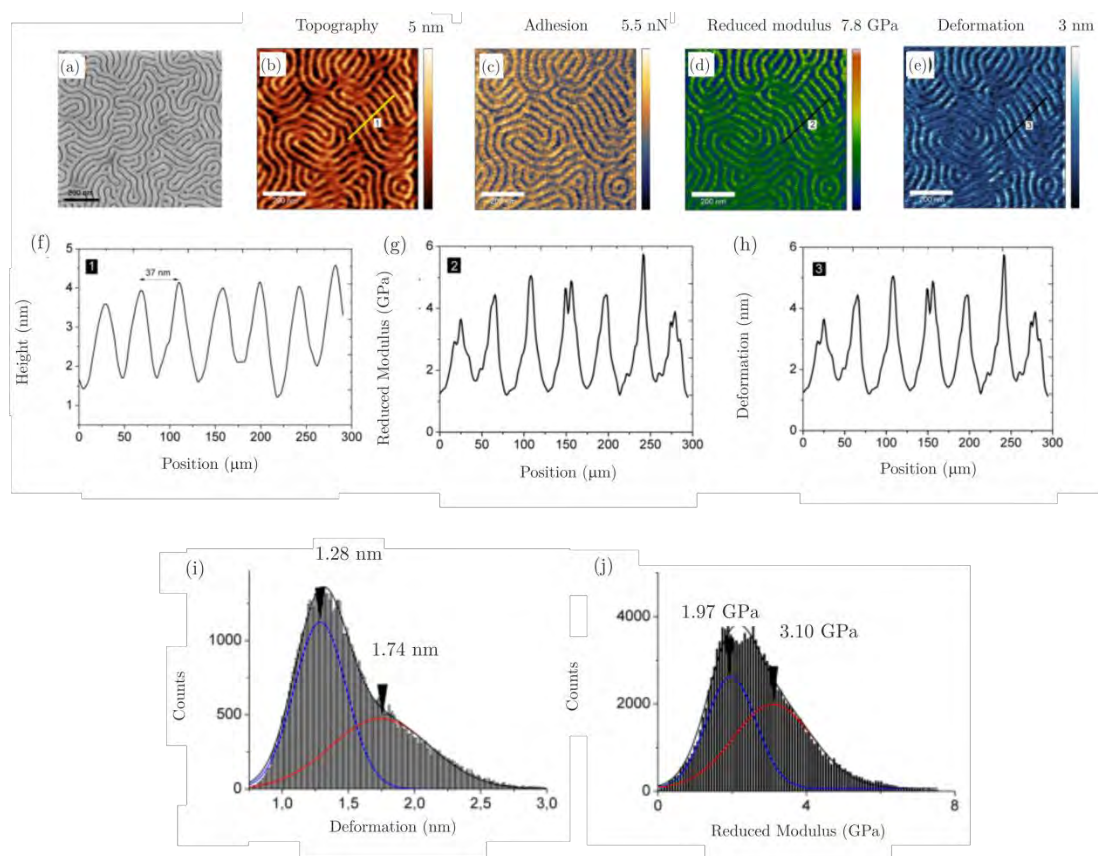

Figure 7.16. (a) SEM image of PS-*b*-PMMA (L_0 = 38 nm) self-assembly, and (b) height, (c) adhesion, (d) reduced modulus, and (e) deformation maps of the sample acquired by peak force at 30 nN set-point. Detailed profiles of (f) height, (g) reduced modulus and (h) deformation. For deformation and elastic maps, the corresponding Gaussian fitting of the data histograms (i) and (j), respectively

7.3.4. Characterization PS-*b*-PMMA thin films after atomic layer deposition

In order to compare the enhancement of mechanical properties with self-assembled layers after ALD, the BCP reference sample has been compared to self-assembled layers exposed to 3, 6 and 9 ALD cycles.

Figure 7.17.a-d shows AFM topography images of PS-*b*-PMMA samples before and after different alumina cycles deposition. Figure 7.17.e shows an histogram with the height distribution of the sample, after 9 ALD cycles. The height difference observed is approximately 2.70 nm. However, to this value, 1.35 nm have to be subtracted due to the initial height difference between phases, and 0.40 nm due to the deformation. This leads to 0.95 nm of alumina that remains on top of PMMA after 9 ALD cycles.

On the other hand, Figure 7.20 shows the reduced modulus maps and the corresponding data histograms of PS-*b*-PMMA samples before and after different alumina cycles deposition. From the graphs, it is clearly observed how stiffness increases locally only on PMMA domains (from 3 to 10 GPa), while the PS elastic response remains unchanged.

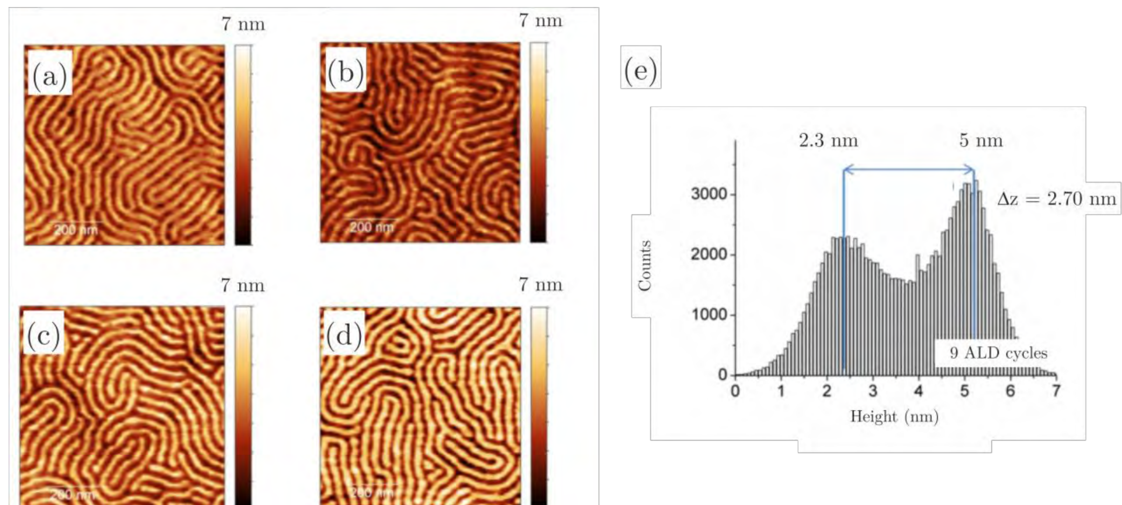

Figure 7.17. AFM topography images of (a) PS-*b*-PMMA, (b) PS-*b*-PMMA + 3 ALD, (c) PS-*b*-PMMA + 6 ALD and (d) PS-*b*-PMMA + 9 ALD. An histogram showing the height distribution of sample PS-*b*-PMMA + 9 ALD, is presented in (e)

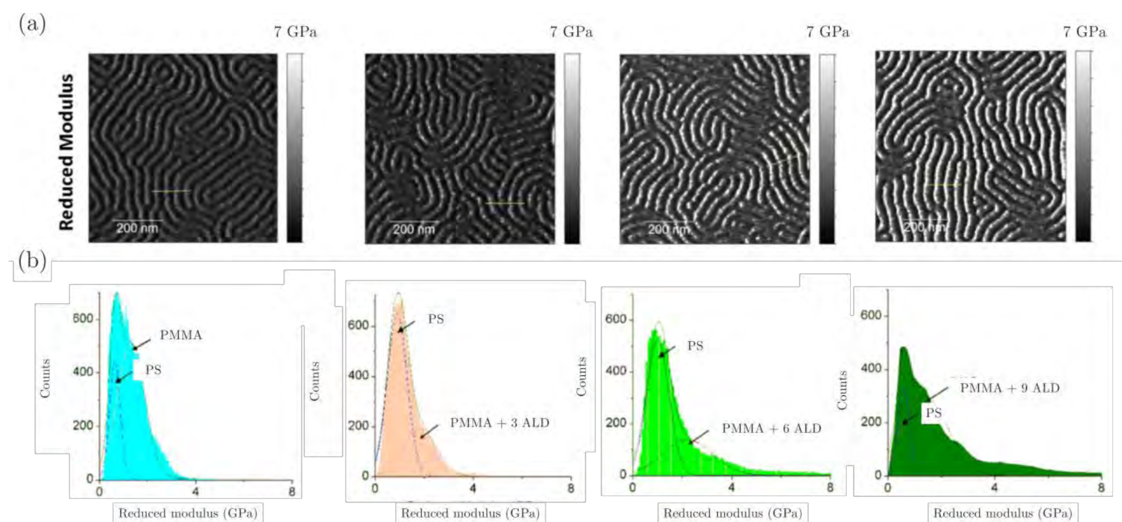

Figure 7.18. (a) AFM elastic maps of PS-*b*-PMMA, PS-*b*-PMMA + 3 ALD, PS-*b*-PMMA + 6 ALD and PS-*b*-PMMA + 9 ALD, and (b) the corresponding data histograms

From the mechanical properties characterization, it is concluded that with an accurate tip calibration, and by adjusting the indentation conditions, it is possible to differentiate between PS and PMMA domains in terms of modulus and adhesion forces. Moreover, the average modulus found for PS and PMMA are in agreement with the ones found in the literature. On the other hand, this technique has the unique capability of recognizing local stiffening induced by the deposition of alumina, as demonstrated in samples exposed to various ALD cycles.[14,25]

7.3.5. Characterization of PS-*b*-PMMA thin films after sequential infiltration synthesis

In order to characterize the difference on the mechanical properties between PS-*b*-PMMA treated with ALD and SIS, infiltrated PS-*b*-PMMA samples are studied.

However, as a first step, infiltrated PS/PMMA blends are investigated on different brush layer materials because after annealing the film dewetts and form micrometer-scale droplets which present the advantage of not needing high lateral resolution. The preparation of the films has been performed by following the procedure described in Figure 3.14, by using PS-OH and PS-*r*-PMMA with 60 and 70% PS content, as brush layers.

As shown in SEM images of Figure 7.19.a-c, the higher the content in PS in the brush, the larger the PS droplets which incorporate smaller PMMA droplets.

On the other hand, the contrast in the SEM cross-section image (Figure 7.19.d), reveals the extent of SIS within PMMA (80-90 nm). The infiltration thickness is less than 200-300 nm, as already reported previously for similar infiltration conditions.[26]

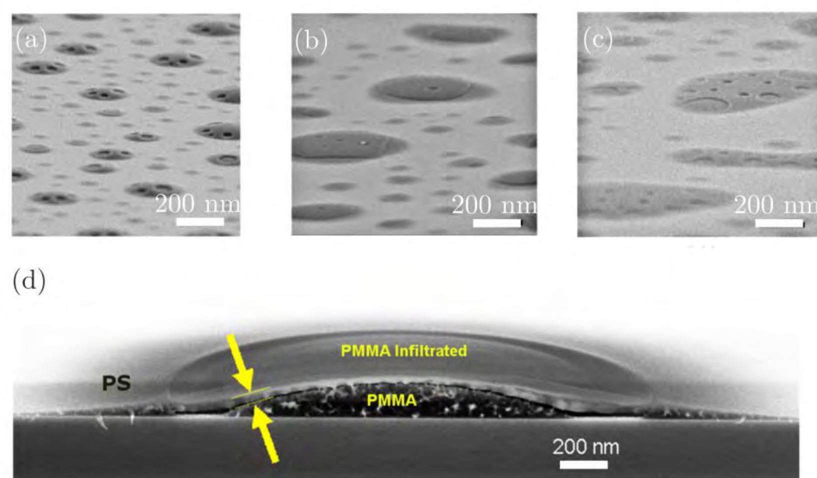

Figure 7.19. SEM images of PS/PMMA droplets on top of (a) PS-OH, (b) $PS_{60\%}$-*r*-PMMA and (c) $PS_{70\%}$-*r*-PMMA and (d) SEM cross-section image of a PS/PMMA droplet on PS-OH after SIS

Then, the local mechanical properties of hPS, hPMMA and homopolymer blend after 5 cycles of SIS are investigated. The results are shown in Figure 7.20. As observed from the modulus profiles, the PMMA modulus increases from 3 to 5.3 GPa after SIS. On the contrary, the PS surface stiffness is less affected changing from 2.6 to 2.2 GPa.

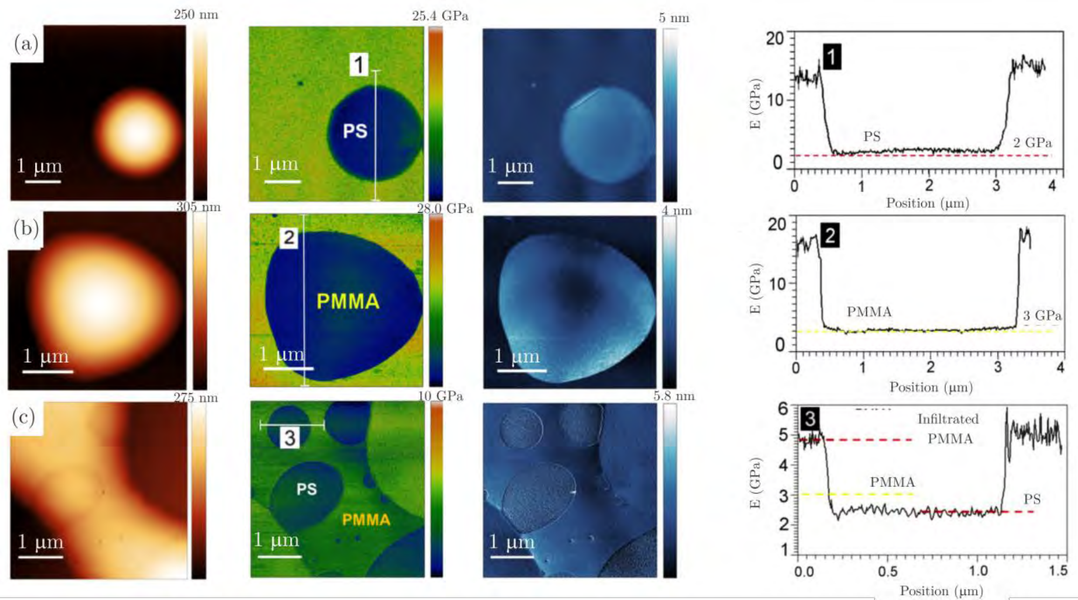

Figure 7.20. Topography, reduced modulus, deformation maps and reduced modulus profiles of (a) PS droplet, (b) PMMA droplet, and (c) infiltrated PS/PMMA droplet

Figure 7.21 shows the results of PS-*b*-PMMA (L_0 = 38 nm) characterization after five cycles of SIS. As observed from the results, there is a modest increase in stiffness on the PMMA domains, after SIS (3.6 GPa). The obtained stiffness is likely to have been due to the creation of an hybrid material in which the alumina is dispersed into a polymeric material.[11]

On the other hand, and compared to the sample exposed to ALD, it has been found that the amount of alumina deposited on the top of PMMA domains is lower because during SIS the alumina is not only deposited on top of PMMA but also infiltrated.

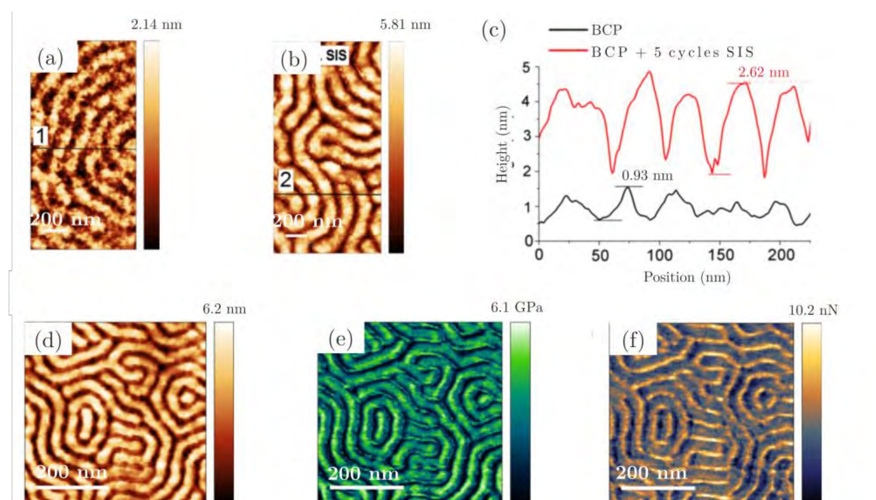

Figure 7.21. AFM topography images of (a) PS-*b*-PMMA and (b) PS-*b*-PMMA + 5 cycles SIS and (c) the corresponding profile; (d-f) represent the topography, modulus and adhesion map, respectively, acquired in Peak Force tapping mode

7.4. Fabrication of nanomechanical devices based on metallic oxide nanowires

As a final objective of the thesis, the fabrication of nanomechanical resonators made of infiltrated polymer as structural material is targeted. The nanofabrication approach is based on using SIS to modify the etching and mechanical properties of the nanowires, together with the DSA of BCP by graphoepitaxy to create the arrays.

Nanomechanical resonators based on suspended nanowires are excellent building blocks since high resonant frequencies can be achieved by reducing the dimensions of the nanowires. Nanowires with sub-10 nm section can show ultrahigh sensitivity when used for the development of mass sensors. Moreover, additional effects arise at such dimensions, like single charge transport effects and quantum phenomena. Recent works at IMB-CNM, demonstrate the realization of a single-hole transistor made of a nanocrystalline suspended p-type silicon nanowire[27], and the onset of enhanced piezoresistive effects[28].

The fabrication of nanomechanical resonators by combining DSA and SIS, allows achieving nanobeam dimensions dictated by half of the BCP pitch. Up to now, nanowires based mechanical resonators have been made of silicon, silicon nitride, carbon nanotubes or 2D materials.[28–31] However, an optimal nanofabrication process in terms of accuracy and scalability is still lacking.

The fabrication process has been performed at the Molecular Foundry (*Lawrence Berkeley National Laboratory*) in Berkeley, CA, EEUU. The Molecular Foundry is supported by the Department of basic energy science, through the Nanoscale Science Research Center program, and it represents a national user facility for nanoscale science which provides users access to expertise and instrumentation in a collaborative, multidisciplinary environment. The Molecular Foundry is organized in seven interdependent research facilities and provides access to state-of-the-art instrumentation, unique scientific expertise and specialized techniques to help users address challenges in nanoscience and nanotechnology.

7.4.1. Materials and methods

7.4.1.1. Description of the fabrication method

The fabrication process to define the nanowire based mechanical resonators is described in Figure 7.22, and it consists on the following steps: (i) fabrication of the topographical guiding patterns on a SOI substrate, (ii) brush layer deposition, (iii) PS-*b*-PMMA self-assembly, (iv) SIS on PMMA domains, (v) PS and brush etching, and (vi) silicon oxide underetching.

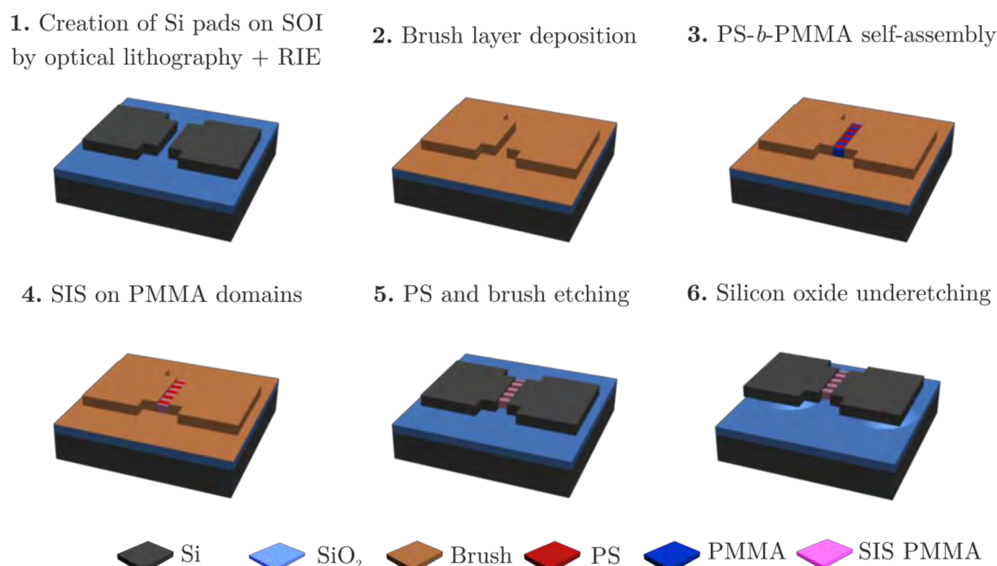

Figure 7.22. Schematic of the nanofabrication process of a device based on an array of identical nanobeams made by DSA and SIS

The creation of the topographical guiding patterns has been performed at the IMB-CNM cleanroom facility by following the process depicted in Figure 4.11 in *chapter 4* on SOI substrates (120 nm silicon on 400 nm SiO_2). After photolithography and development steps, 120 nm of silicon have been etched down to the SiO_2 layer by using the etching conditions depicted in Table 4.2.

7.4.1.2. Brush and block copolymer materials

The BCP and brush materials used in the experiments are summarized in Table 7.3. The brush is deposited on the guiding patterns from a 2% $PS_{60\%}$-*r*-PMMA solution at 1500 rpm, and annealed at 230°C for 5 min, covering the whole surface. Then, the sample is dipped in PGMEA for 5 min at 40°C in an ultrasonic bath. Finally, 0.5% PS-*b*-PMMA solution is spin-coated at 2500 rpm, and annealed at 230°C for 10 min.

Table 7.3. Specifications of PS-*b*-PMMA and brush materials (* BCP blend formed of a mixture of 38 nm and 22 nm BCP pitch (40:60))

Chemical nature	M_n	PDI	PS fraction	Pitch
$PS_{60\%}$-*r*-PMMA	7.9 kg/mol	1.85	60%	-
PS-*b*-PMMA	79 kg/mol	1.09	50%	38 nm
	Blend*			28 nm
	42.3 kg/mol	1.1		22 nm

7.4.1.3. Directed self-assembly by graphoepitaxy process

The same graphoepitaxy experiments performed with PS-*b*-PMMA of 22 nm pitch and described in *chapter 4*, have been replicated at the Molecular Foundry, and the results have been the same as those presented in Figure 4.8.

On the other hand, the process has been also tried with two more BCP, showing good alignment for the 28 nm pitch BCP (Figure 7.23).

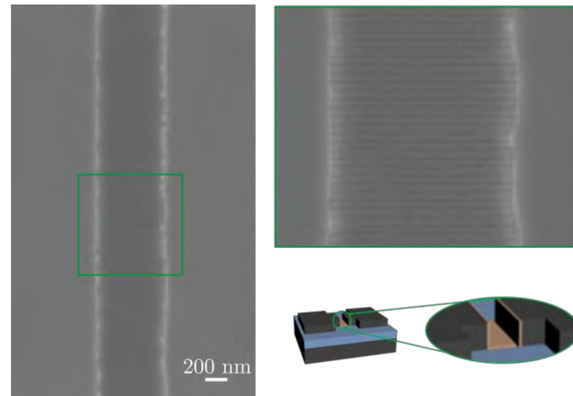

Figure 7.23. PS-*b*-PMMA (L_0 = 28 nm) DSA by graphoepitaxy by using 600 nm separation width

7.4.1.4. Optimization of sequential infiltration synthesis in free-surface

In parallel to the DSA optimization, the SIS process has been optimized in a new ALD tool at the Molecular Foundry (*Maxima SMD VI*). The process optimization has been performed on PS-*b*-PMMA samples on free-surface for two materials: Al_2O_3 and ZnO.

Sequential infiltration synthesis with Al_2O_3

In order to optimize the SIS process, a first test has been performed on PS-*b*-PMMA of 38 nm pitch, and based on the obtained results, the precursor pulse, the temperature and the purge time have been varied. This sequence is illustrated in Figure 7.24.

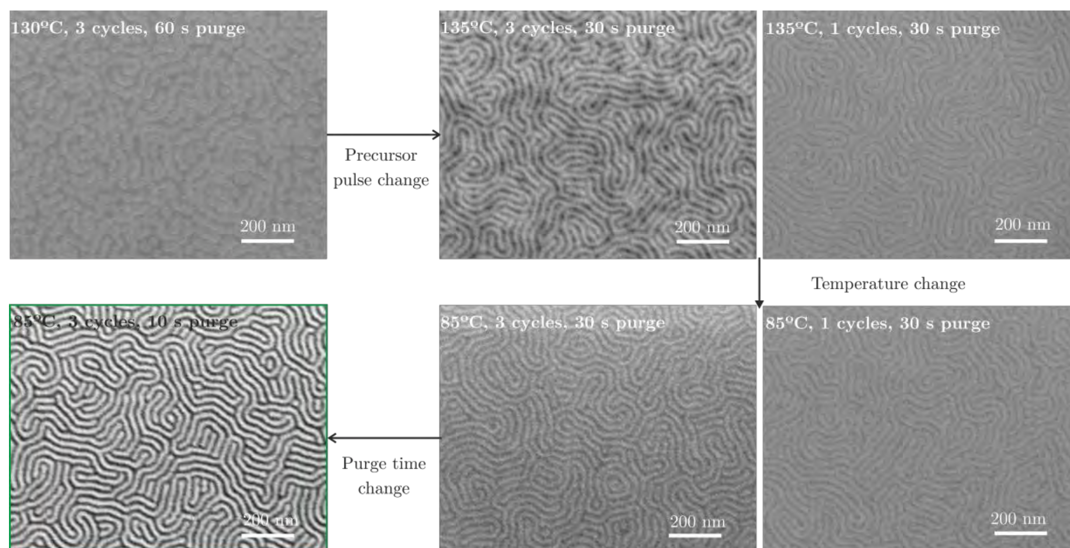

Figure 7.24. Sequence followed to optimize the SIS with Al_2O_3 on PS-*b*-PMMA (L_0 = 38 nm)

Once the optimal SIS conditions have been found, they have been transferred to the other two BCP (L_0 = 22 nm and 28 nm). Then, the SIS process has been characterized as a function of the different experimental parameters (number of cycles, purge times, BCP film

thickness and BCP molecular weight). All the experiments have been performed by using the optimal conditions (85°C, 3 cycles and 10 s of purge) and by varying only the parameter of study.

Figure 7.25 shows the SIS dependence as a function of the number of cycles. As observed from the SEM images, one cycle is not enough to infiltrate the whole PMMA domains, therefore poor contrast is observed. On the other hand, for cycles above 5, alumina deposition is started to be seen on the fingerprint morphology.

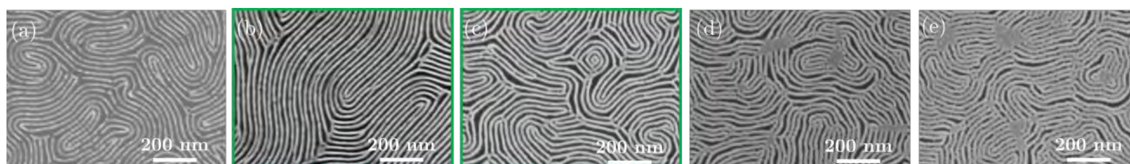

Figure 7.25. SIS with Al_2O_3 on PS-*b*-PMMA (L_0 = 22 nm) as a function of the number of cycles: (a) one, (b) three, (c) five, (d) seven and (e) nine (SEM images have been taken after PS removal)

Figure 7.26 shows the SIS results when varying the purge time after the precursor reaction inside the chamber. As revealed in the images, the best results are obtained for purge times of 10 s. Above this time, the SIS is not so efficient and partially infiltrated areas appear, in accordance with the literature.[11]

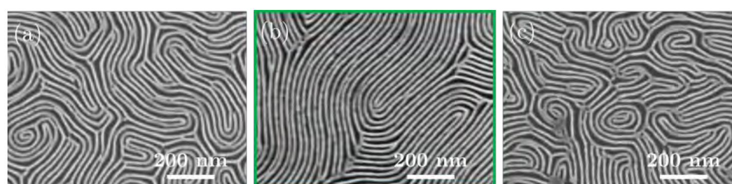

Figure 7.26. SIS with Al_2O_3 on PS-*b*-PMMA (L_0 = 22 nm) as a function of the purge time: (a) 5 s, (b) 10 s and (c) 30 s (SEM images have been taken after PS removal)

Then, BCP of different film thickness have been infiltrated. Since the orientation of the lamellae depends on the BCP thickness, there are some samples (Figure 7.27.c-d) which show some parallel oriented lamellae before the SIS process. The results after SIS are shown in Figure 7.27, and for the two perpendicular oriented samples (Figure 7.27.a-b), a decrease in contrast in the thickest BCP sample (Figure 7.27.b) is observed. On other hand, it is observed, that the alumina is deposited on the parallel oriented lamellae (Figure 7.27.c-d).

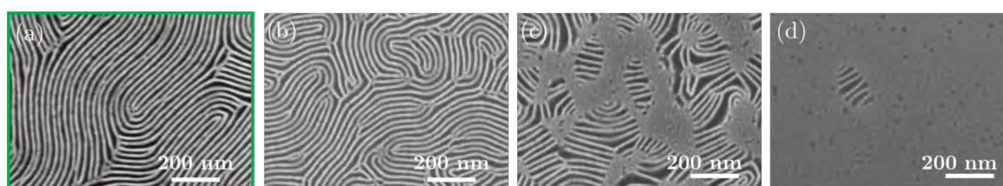

Figure 7.27. SIS with Al_2O_3 on PS-*b*-PMMA (L_0 = 22 nm) as a function of BCP film thickness (SEM images have been taken after PS removal)

On the other hand, the SIS with Al_2O_3 has been performed on three molecular weight BCPs by using the optimal conditions described above. As revealed in the SEM images of Figure 7.28, there is no influence on the process when varying the BCP chain length within the chosen values (from 22 to 38 nm).

Figure 7.28. SIS with Al_2O_3 on PS-*b*-PMMA as a function of BCP chain length: (a) 38 nm, (b) 28 nm, and (c) 22 nm (SEM images have been taken after PS removal)

Finally, in order to demonstrate the influence of the purge time and the temperature on the final BCP structure, the sample infiltrated at 85°C, with 1 SIS cycle and 10 s purge time from Figure 7.25.a, has been compared with a sample processed under the same conditions but with higher purge times and higher temperature. Figure 7.29.a and Figure 7.29.b, show the difference on the infiltration depending on the purge time. As observed, and as demonstrated before, the higher the purge times, the less infiltrated the sample is (it is revealed by the poor contrast on the SEM image). On the other hand, when comparing Figure 7.29.a and Figure 7.29.c, in which the temperature has been increased to 135°C, it is observed that the infiltration process works much better, driving to the same results as those in which the sample is infiltrated for 3 cycles at 85°C.

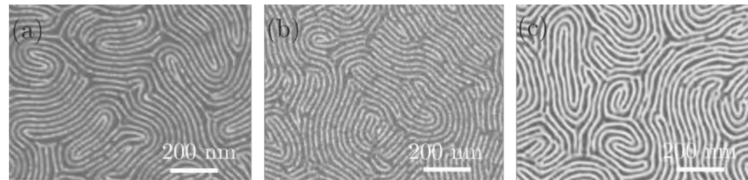

Figure 7.29. SIS with Al_2O_3 on PS-*b*-PMMA for 1 cycle and (a) 85 °C, 10 s purge time, (b) 85°C, 30 s purge time, and (c) 135°C, 10 s purge time

<u>*Sequential infiltration synthesis with ZnO*</u>

In addition to Al_2O_3, the infiltration using another oxide of interest, namely ZnO, has been also performed. This material has been chosen due to its many advantageous properties, such as thermal and electrical stabilities and optical transparency.[32,33] Moreover, it presents a wide band gap of 3.37 eV, a large exciton binding energy of 60 meV, and its structure leads to large piezoelectricity.[34–36]

The ALD process for ZnO uses diethylzinc (DEZ) and water as precursors. The reaction mechanism process consists of the reactions (7.7) and (7.8).

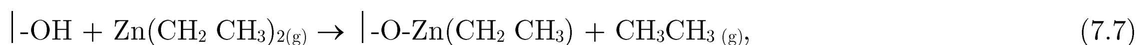

$$|\text{-OH} + Zn(CH_2\,CH_3)_{2(g)} \rightarrow |\text{-O-}Zn(CH_2\,CH_3) + CH_3CH_{3\,(g)}, \quad (7.7)$$

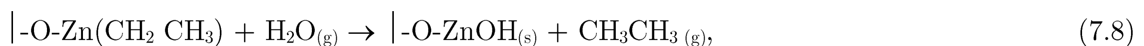

$$|\text{-O-}Zn(CH_2\,CH_3) + H_2O_{(g)} \rightarrow |\text{-O-}ZnOH_{(s)} + CH_3CH_{3\,(g)}, \quad (7.8)$$

In order to infiltrate ZnO into the PMMA domains, the process has been tried by using the same processing conditions found for Al_2O_3. As observed in Figure 7.30, the SEM images after PS etching reveal that the infiltration has failed, and almost all the BCP film has been removed.

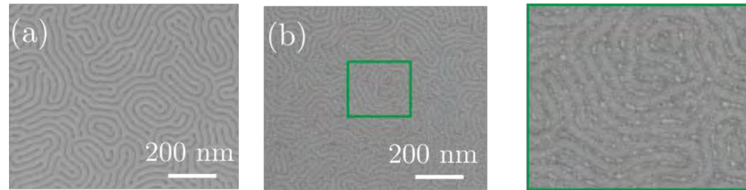

Figure 7.30. SEM images of PS-*b*-PMMA (L_0 = 38 nm) + 3 cycles of SIS (ZnO) (a) before and (b) after PS etching

Therefore, in order to promote the ZnO infiltration, different approaches have been tried. On the one hand, the activation and slightly oxidization of the surface has been tested, before the SIS process, by exposing the sample to a short time of oxygen plasma or UV. As observed, in Figure 7.31, the process has not worked, and only some infiltrated regions remain after PS etching.

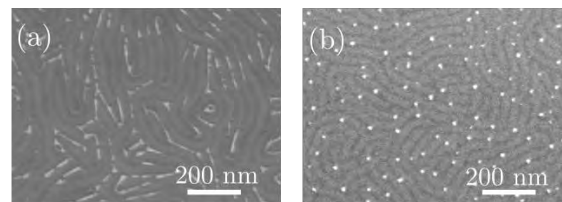

Figure 7.31. SEM images of PS-*b*-PMMA (L_0 = 38 nm) with smooth (a) oxygen plasma and (b) UV exposure, + 3 cycles of SIS (ZnO) after PS etching

Another approach that has been tried consists in infiltratating one Al_2O_3 cycle before 3 ZnO SIS cycles, in order to activate the surface and promote the ZnO growth on an alumina layer. The process has been performed at 85°C with 10 s of purge time, and the result obtained is presented in Figure 7.32. As observed in the images, the process works when the surface is first infiltrated with alumina. Moreover, the higher contrast shown in Figure 7.32.a, if compared with Figure 7.25.a, reveals that there is ZnO infiltration. Moreover, in the SEM cross-section image, Figure 7.32.b, two contrasted phases corresponding to Al_2O_3 and ZnO, are observed.

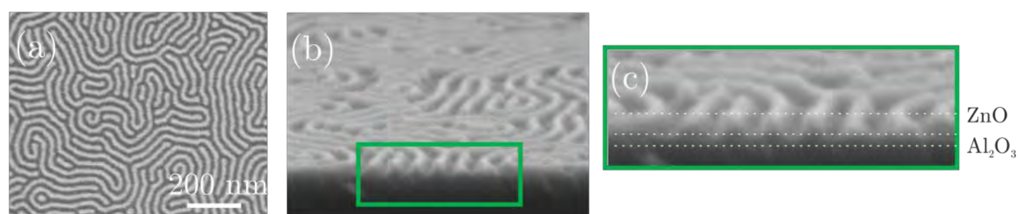

Figure 7.32. (a) Top-view and (b) cross-section SEM image and (c) inset of PS-*b*-PMMA (L_0 = 38 nm) with one Al_2O_3 and three ZnO cycles after PS etching

Finally, in order to demonstrate the ZnO infiltration without using Al_2O_3 activation, since the temperature has demonstrated to increase the reaction speed, the procedure has been tried at higher temperatures (Figure 7.33). On the other hand, by keeping constant the temperature at 85°C, the experiment has been performed by changing the order of the precursors introduction in the chamber. That is, the water has been introduced first, and then, the DEZ (Figure 7.34). As observed in both figures, the increasing temperature enhances the SIS process, and a thin infiltrated PMMA layer remains on the substrate after PS etching. On the other hand, the infiltration enhances more when the sequence of introducing the precursors inside the chamber is inverted. The reason behind is that water reacts more with PMMA carbonyl groups than DEZ does, and therefore leaves more reactive sites when DEZ is introduced in the chamber.

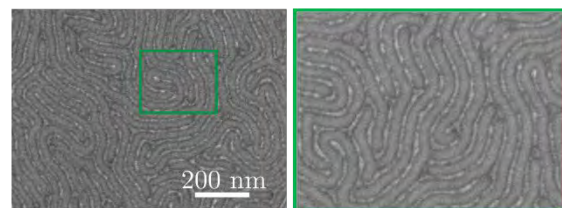

Figure 7.33. SEM image of PS-*b*-PMMA (L_0 = 38 nm) with three ZnO cycles at 135°C after PS etching

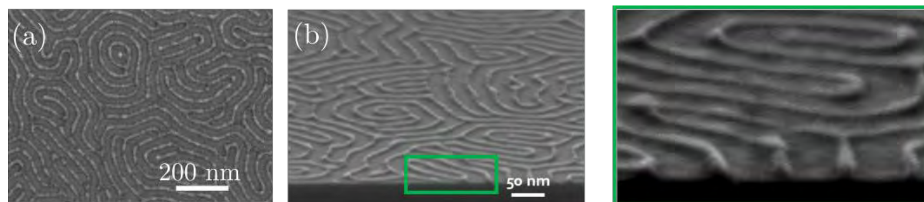

Figure 7.34. SEM image of PS-*b*-PMMA (L_0 = 38 nm) with three ZnO cycles at 85°C by inverting the introduction of precursors into the chamber

7.4.2. Nanomechanical resonators fabrication results

Once the SIS process on free-surface is optimized for both Al_2O_3 and ZnO materials, it is combined with the DSA by graphoepitaxy to fabricate the nanobeams. Figure 7.35 shows the DSA results for PS-*b*-PMMA of 28 nm pitch after infiltration, before and after PS etching. On the other hand, Figure 7.36 shows a SEM 30° tilted image of Figure 7.35.b. As observed, the beams are already suspended after PS etching, since the infiltration does dot diffuse through the whole PMMA domains down to the bottom.

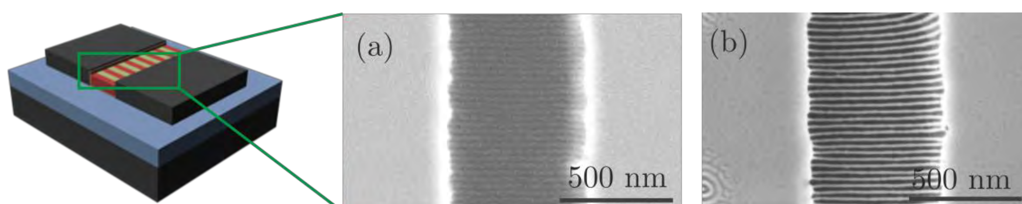

Figure 7.35. SEM images of PS-*b*-PMMA (L_0 = 28 nm) with three Al_2O_3 cycles at 85°C (a) before and (b) after PS etching

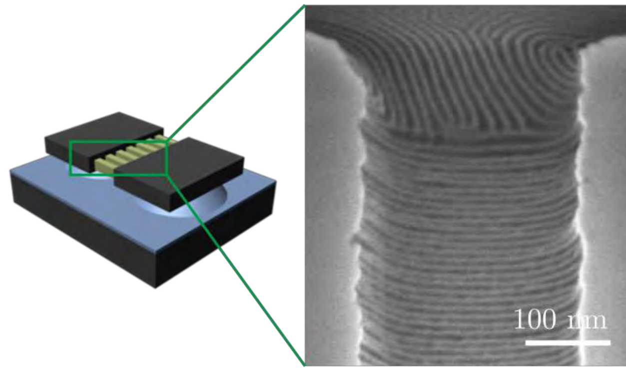

Figure 7.36. SEM 30° tilted image of PS-*b*-PMMA (L_0 = 28 nm) with three Al_2O_3 cycles at 85°C after PS etching

The PS etching step has to be accurately controlled since the nanowires tend to crosslink between them at longer oxygen plasma exposures. Figure 7.37 shows this effect after 10 min of oxygen plasma etching.

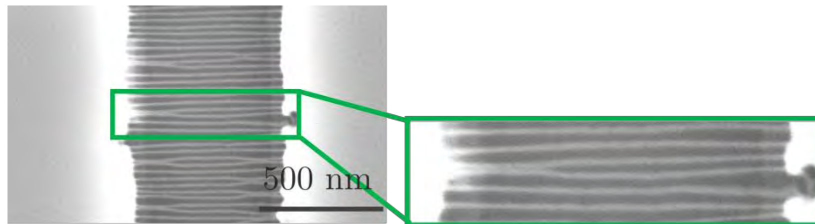

Figure 7.37. SEM image of PS-*b*-PMMA (L_0 = 28 nm) with three Al_2O_3 cycles at 85°C after 10 min PS etching

To corroborate that the nanowires are suspended after the optimal PS etching removal time (Figure 7.35.b), a SEM cross-section at 90° has been taken. As observed in Figure 7.38, the Al_2O_3 infiltrated nanowires are already suspended after the PS etching since the infiltration does not reach the bottom of the PMMA domain. Therefore, there is no need to go further and etch the SiO_2 under-layer to suspend them.

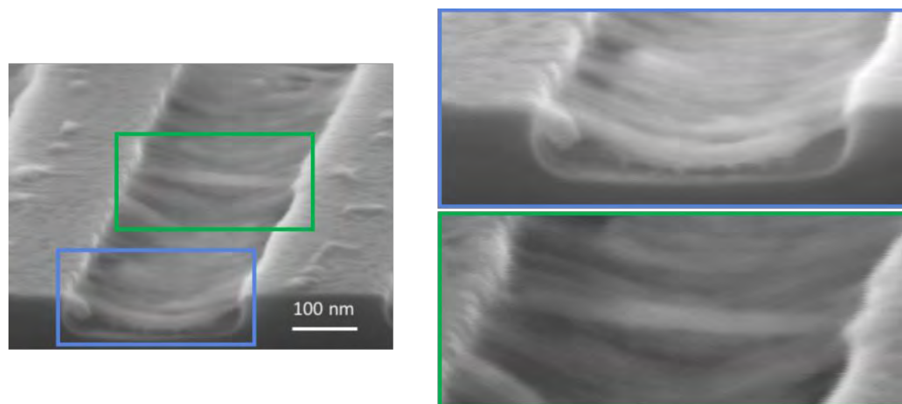

Figure 7.38. SEM image of PS-*b*-PMMA (L_0 = 28 nm) with three Al_2O_3 cycles at 85°C after 2 min PS etching showing the suspended infiltrated nanowires

Finally, the same procedure has been tried not with alumina, but with the optimal infiltration conditions found for ZnO. As observed in Figure 7.39, after the PS etching, very few nanowires stand after PS etching. However, the remaining can be used to measure some of their properties.

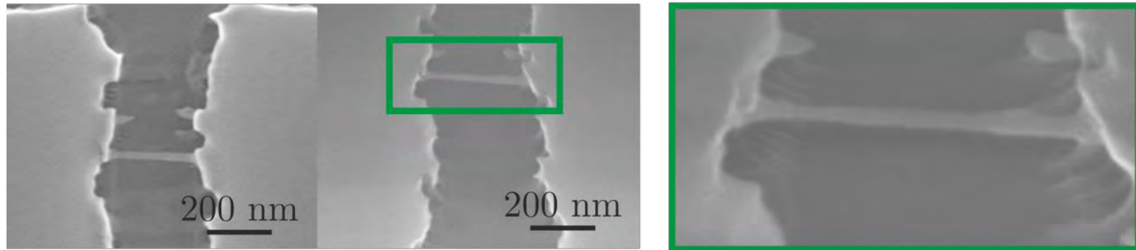

Figure 7.39. SEM image of PS-*b*-PMMA (L_0 = 28 nm) with three ZnO cycles at 85°C after 2 min PS etching showing the suspended infiltrated nanowires

In order to enhance the results shown in Figure 7.39 it is possible to increase the number of ZnO infiltration cycles, or repeat the procedure increasing also the temperature.

7.5. Summary and conclusions

A reliable method to pattern transfer BCPs has been implemented for BCP DSA. Moreover, the difference between the conventional ALD process and SIS has been presented and corroborated by an extensive study on the mechanical properties of the BCP after the treatments. The difference between processing conditions is depicted in Table 7.4.

Table 7.4. Optimal processing conditions for ALD and SIS

Conditions	ALD	SIS
Temperature	85°C	85°C
Precursor time in the chamber	60 s	80 s
Purge time	60 s	30 s
Cycles	5 cycles	5 cycles

The SIS process has been tried not only for PS-*b*-PMMA materials, but also for high-χ systems. It has been demonstrated that the infiltration process in PLA domains has a similar mechanism as for PMMA, due to the carbonyl groups found in PLA molecular structure.

Apart from Al_2O_3, ZnO has been also tried as infiltrating material. However, due to the reactivity of the precursors with the PMMA molecules, the infiltration procedure needs to be performed at higher temperatures and with a higher number of cycles. On the other side, it has been observed, that the change on the order the precursors are introduced into the chamber enhances the infiltration process.

From the mechanical characterization, it has been found that ALD and SIS enhance the stiffness of PMMA domains, while PS remains almost constant. Furthermore, it has been demonstrated that in ALD, there is only material deposition whereas in SIS not only deposition, but infiltration as well. This is also demonstrated in the etching tests performed with both techniques.

On the other hand, the application of BCP DSA and SIS has been combined to fabricate nanomechanical resonators which can be used on the development of mass sensors. It has been demonstrated that DSA, in combination with SIS, is a powerful technique in that field, since it provides the resolution of half of the BCP pitch, by using a simple and affordable process. However, further work has still to be performed on the fabrication process optimization and nanowire characterization.

7.6. References

1. A. M. Shevjakov, *et al.* Chemistry of High-Temperature Materials. *Proc. 2nd USSR Conf. High Temp. Chem. Oxides* **26–29,** 149–155 (1965).

2. Suntola, T. *et al.* Method for producing compound thin films. (1977).

3. McDaniel, M. D. *et al.* Atomic layer deposition of perovskite oxides and their epitaxial integration with Si, Ge, and other semiconductors. *Appl. Phys. Rev.* **2,** 41301 (2015).

4. Purniawan, A., *et al.* TiO2 ALD nanolayer as evanescent waveguide for biomedical sensor applications. *Procedia Eng.* **5,** 1131–1135 (2010).

5. Puurunen, R. L. Surface chemistry of atomic layer deposition: A case study for the trimethylaluminum/water process. *J. Appl. Phys.* **97,** 121301 (2005).

6. Parsons, G. N. *et al.* Mechanisms and reactions during atomic layer deposition on polymers. *Coord. Chem. Rev.* **257,** 3323–3331 (2013).

7. Peng, Q., *et al.* Nanoscopic patterned materials with tunable dimensions via atomic layer deposition on block copolymers. *Adv. Mater.* **22,** 5129–5133 (2010).

8. Krishnamoorthy, *et al.* Nanoscale patterning with block copolymers. *Mater. Today* **9,** 40–47 (2006).

9. Huda, M., *et al.* Pattern Transfer of 23-nm-Diameter Block Copolymer Self-Assembled Nanodots Using CF 4 Etching with Carbon Hard Mask (CHM) as Mask. **737,** 133–136 (2013).

10. Tseng, Y.-C., *et al.* Enhanced Block Copolymer Lithography Using Sequential Infiltration Synthesis. *J. Phys. Chem. C* **115,** 17725–17729 (2011).

11. Biswas, M., *et al.* Kinetics for the Sequential In fi ltration Synthesis of Alumina in Poly(methyl methacrylate): An Infrared Spectroscopic Study. (2015).

12. Biswas, *et al.* New Insight into the Mechanism of Sequential In fi ltration Synthesis from Infrared Spectroscopy. (2014).

13. Tseng, Y. C., *et al.* Enhanced block copolymer lithography using sequential infiltration synthesis. *J. Phys. Chem. C* **115,** 17725–17729 (2011).

14. Lorenzoni, M., Evangelio, L., *et al.* Assessing the Local Nanomechanical Properties of Self-Assembled Block Copolymer Thin Films by Peak Force Tapping. (2015).

15. Darling, S. B., *et al.* Sequential infiltration synthesis for advanced lithography. (2012).

16. Peng, Q., *et al.* A route to nanoscopic materials via sequential infiltration synthesis on block copolymer templates. *ACS Nano* **5,** 4600–4606 (2011).

17. Johnston, D. E. Plasma etch transfer of self-assembled polymer patterns. *J. Micro/Nanolithography, MEMS, MOEMS* **11,** 31306 (2012).

18. Ruiz, R. *et al.* Image quality and pattern transfer in directed self assembly with block-selective atomic layer deposition. *J. Vac. Sci. Technol. B, Nanotechnol. Microelectron. Mater. Process. Meas. Phenom.* **30,** 06F202 (2012).

19. Young, T. J. *et al.* The use of the PeakForce TM quantitative nanomechanical mapping AFM-based method for high-resolution Young's modulus measurement of polymers. *Meas. Sci. Technol.* **22,** 125703 (2011).

20. Cappella, B. *et al.* Nanomechanical properties of polymer thin films measured by force–distance curves. *Thin Solid Films* **516,** 1952–1960 (2008).

21. Du, B., *et al.* Study of Elastic Modulus and Yield Strength of Polymer Thin Films Using Atomic Force Microscopy. *Langmuir* **17,** 3286–3291 (2001).

22. Oommen, B. *et al.* Effects of nanoscale thickness and elastic nonlinearity on measured mechanical properties of polymeric films. *Thin Solid Films* **513,** 235–242 (2006).

23. Cappella, B. *et al.* Force-distance curves by atomic force microscopy. *Surf. Sci. Rep.* **34,** 1–104 (1999).

24. Vesenka, J., *et al.* Colloidal gold particles as an incompressible atomic force microscope imaging standard for assessing the compressibility of biomolecules. *Biophysical Journal* **65,** 992–997 (1993).

25. Lorenzoni, M. *et al.* Nanomechanical properties of solvent cast PS and PMMA polymer blends and block co-polymers. *Proc. SPIE* **9423,** 942310–942325 (2015).

26. Tseng, Y.-C. *et al.* Enhanced polymeric lithography resists via sequential infiltration synthesis. *J. Mater. Chem.* **21,** 11722–11725 (2011).

27. Llobet, J. *et al.* Resonant tunnelling features in a suspended silicon nanowire single-hole transistor. *Appl. Phys. Lett.* **107,** 1–6 (2015).

28. Sansa, M., *et al.* High-sensitivity linear piezoresistive transduction for nanomechanical beam resonators. *Nat. Commun.* **5,** 4313 (2014).

29. Eichler, A. *et al.* Nonlinear damping in mechanical resonators made from carbon nanotubes and graphene. *Nat. Nanotechnol.* **6,** 339–342 (2011).

30. Gil-Santos, E. *et al.* Nanomechanical mass sensing and stiffness spectrometry based on two-dimensional vibrations of resonant nanowires. *Nat. Nanotechnol.* **5,** 641–645 (2010).

31. Fong, K. Y., *et al.* Frequency and phase noise of ultrahigh Q silicon nitride nanomechanical resonators. *Phys. Rev. B - Condens. Matter Mater. Phys.* **85,** 1–5 (2012).

32. Ott, A. W. *et al.* Atomic layer-controlled growth of transparent conducting ZnO on plastic substrates. *Mater. Chem. Phys.* **58,** 132–138 (1999).

33. Kowalik, I. A. *et al.* Structural and optical properties of low-temperature ZnO films grown by atomic layer deposition with diethylzinc and water precursors. *J. Cryst. Growth* **311,** 1096–1101 (2009).

34. Wang, Z. L. ZnO nanowire and nanobelt platform for nanotechnology. *Mater. Sci. Eng. R Reports* **64,** 33–71 (2009).

35. Wang, C. Y. *et al.* ZnO-CNT composite nanotubes as nanoresonators. *Phys. Lett. Sect. A Gen. At. Solid State Phys.* **375,** 2171–2175 (2011).

36. Korir, K. K., *et al.* Piezoelectric properties of zinc oxide nanowires: an *ab initio* study. *Nanotechnology* **24,** 475401 (2013).

General conclusions

The thesis contributes to the development of directed self-assembly of block copolymers as a fabrication method for the next generation of nanoelectronic devices and circuits.

The primary achievement has been the development, implementation and characterization of a chemical epitaxy process for PS-*b*-PMMA systems.

- The DSA chemical epitaxy process is based on creating a chemical nanoscale contrast on a polymeric brush layer by oxygen plasma functionalization.

  The optimal processing conditions for brush and BCP preparation, guiding pattern definition by EBL and oxygen plasma functionalization, have been established. This has entailed the study of different brush layer compositions and BCP annealing conditions, required for each specific system.

  It has been successfully implemented to lamellar forming PS-*b*-PMMA BCPs of the following periods: 38 nm, 28 nm and 22 nm. Density multiplication factors up to 7 have been achieved by means of using wide guiding stripes. It has been demonstrated that the use of wide guiding stripes is of prime importance in chemical epitaxy since it allows relaxing the lithography requirements in terms of resolution, enabling furthermore, the process integration to high-χ systems.

  It has been investigated the role of the interface energies between the brush and the BCP domains by a novel experimental method based on using homopolymer blends. The contact angle between two phases in droplets formed by homopolymer blend dewetting experiments on brush layers is related with the affinity strength. The experimental data has been fitted in a DSA model to simulate the chemical epitaxy process, and a good experimental correlation has been obtained. From simulation results it is proposed that, along with the difference on surface free-energies, a relevant parameter to define the efficiency of the guiding patterns to obtain standing lamellae oriented parallel to the guiding patterns is the responsiveness of the brush layer, which is related with the brush density.

Along with the characterization and development of a chemical epitaxy approach, other complementary methods and exploratory investigations have been addressed.

- It has been studied the self-assembly behavior of two novel high-χ materials: PS-*b*-PLA and PLA-*b*-PDMS-*b*-PLA.

  With respect to PS-*b*-PLA, a proper brush layer which balances the interactions between the surface and the BCP domains has been found, thus leading to the perpendicular BCP orientation on the whole surface. Moreover, the self-assembly behavior has been studied by using short thermal annealing times, demonstrating thus, its easy industrial applicability. A DSA chemical epitaxy process for PS-*b*-PLA has been partially achieved. A chemical contrast to force the alignment of the domains has been observed, but not strong enough to guide them parallel to the guiding stripes.

  Regarding the PLA-*b*-PDMS-*b*-PLA system, a DSA process has been implemented using a novel approach based on the combination of grapho and chemical epitaxy, showing large areas with high density multiplication factors. Furthermore, this BCP has shown very remarkable DSA results with respect to integration capability.

- Two new chemical epitaxy processes based on direct writing techniques have been designed and implemented for PS-*b*-PMMA material systems. The guiding patterns on the two processes have been created by locally oxidizing the surface with AFM nanolithography, and by exposing the sample directly to the electron beam. The development of these methods has allowed simplifying the processing sequence steps, since the use of resists is avoided, and obtaining guiding patterns of higher resolution (smaller linewidth).

- It has been implemented a sequential infiltration synthesis (SIS) to enhance the etch resistivity between PS and PMMA. This process improves the pattern transfer into the substrate. It has been demonstrated for PS-*b*-PMMA, for high-χ systems and for two different infiltration materials, Al_2O_3 and ZnO. The combination of BCP DSA by graphoepitaxy and SIS has been applied to the design and fabrication of nanomechanical resonators for mass sensing applications. As the nanowires are created directly from the infiltrated polymer domain, the advantage of this process is that nanowires of very small cross-section can be obtained.

- Two techniques to further characterize BCP films and their interactions with the substrate have been presented.

It has been demonstrated that Hard X-ray Photoelectron Spectroscopy (HAXPES) using synchrotron radiation is a powerful technique to explore the chemical properties of the surface and buried interfaces in the DSA process.

Three chemical guiding patterns have been characterized, and the subsequent modifications performed on the brush polymer have been identified. It has been demonstrated that when the brush is exposed to oxygen plasma, it generates C-O bonding, promoting higher affinity to PMMA domains. In case of Parallel Oxidation Nanolithography (PON), it has been seen that a sub-stoichiometric oxide appears between the brush and the substrate. When the polymer is exposed to electrons, the cross-linking of PS molecules is what induces the BCP alignment.

Characterization by Atomic Force Microscopy (AFM) using the peak force quantitative nanomechanical mode has made possible to access the local mechanical properties of the single BCP domains, surpassing the limitations of standard nanoindentation methods. Quantitative information about the average modulus of PS and PMMA on PS-*b*-PMMA films has been obtained. This technique has been also applied to PS-*b*-PMMA infiltrated BCPs, showing the unique capability of the method in recognizing local stiffening induced by the deposition and infiltration of alumina, as well as its evolution in terms of thickening and stiffening as a function of the numbers of ALD cycles.

In summary, the research performed within this thesis contributes significantly to the DSA community, since it demonstrates a feasible industrial implementation of a new chemical epitaxy approach for PS-*b*-PMMA BCPs, as well as the chemical mechanism which drives their DSA. Moreover, a broad study on new novel BCPs has been performed, providing a general overview of the major drawbacks and advantages of their implementation in the industry, as well as a possible DSA fabrication process to their integration. The fabrication process of a nanomechanical resonator has been presented by combining the DSA technology with SIS.

Conclusions generals

Aquesta tesi contribueix al desenvolupament de l'auto-assemblatge dirigit de copolímers de bloc com a mètode de fabricació per a la futura generació de dispositius i circuits nanoelectrònics.

La principal contribució ha estat el desenvolupament, implementació i caracterització d'un mètode de guiatge basat en la modificació química de la superfície per als copolímers de bloc basats en PS-*b*-PMMA.

- El procés de guiatge per modificació química de la superfície, es basa en crear un contrast químic nanomètric a una capa de polímer, a través de la seva modificació amb plasma d'oxigen.

  S´han establert les condicions de procés òptimes per a la preparació de la capa de copolímer de bloc i la corresponent definició dels patrons de guiatge per litografia amb feix d'electrons i modificació amb plasma d'oxigen. Això ha comportat realitzar un profund estudi amb diferents polímers i condicions de recuit, requerides per a cada sistema.

  S'ha demostrat, la implementació del copolímer laminar PS-*b*-PMMA amb les següents longituds de cadena: 38 nm, 28 nm i 22 nm, i s'han obtingut factors de multiplicació fins a 7, utilitzant línies àmplies de guiatge. S'ha demostrat que l'ús de línies amples de guiatge és molt important en l'estudi de l'auto-assemblatge dirigit de copolímers de bloc per modificació química de la superfície, perquè això permet relaxar els requeriments litogràfics en termes de resolució, permetent alhora, la integració dels sistemes d'alta χ.

  S'ha investigat el paper de les energies d'interfície entre la capa de polímer "brush" i els dominis del copolímer, mitjançant un nou mètode basat en l'ús d'una mescla d'homopolímers. Mitjançant la mesura de l'angle de contacte entre les dues fases d'una gota formada per una mescla d'homopolímers, és possible determinar l'afinitat química. Les dades experimentals s'han ajustat a un model d'auto-assemblatge dirigit per simular el procés, i s'ha obtingut una bona correlació. Dels resultats de les simulacions s'ha conclòs que juntament amb la diferència d'energies d'interfície, la densitat de la capa de "brush" juga un paper important a l'hora de definir l'eficiència del patró de guiatge per obtenir làmines perpendiculars al substrat i paral · leles a les línies de guiatge.

Juntament amb la caracterització i desenvolupament del mètode de guiatge basat en modificació química de la superfície, també s'han dut a terme altres investigacions.

- S'ha estudiat el mecanisme d'auto-assemblatge de dos materials d'alta χ: PS-*b*-PLA i PLA-*b*-PDMS-*b*-PLA.

  Respecte al sistema PS-*b*-PLA, s'ha trobat una capa neutra de polímer "brush", la qual balança les interaccions entre la superfície i els dominis del copolímer. Això ha donat lloc a una orientació perpendicular del copolímer de bloc a tota la superfície. A més, el procés d'auto-assemblatge s'ha demostrat utilitzant temps curts de recuit tèrmic, demostrant així, la seva fàcil aplicabilitat industril. El procés d'auto-assemblatge dirigit de copolímers de bloc per epitàxia química, s'ha aconseguit de manera parcial, ja que s'ha observat contrast químic a la superfície, però no suficientment fort com per guiar el polímer de manera paral · lela a les línies del patró.

  En referència al sistema PLA-*b*-PDMS-*b*-PLA, s'ha demostrat la implementació d'un nou procés d'auto-assemblatge dirigit, basat en mètodes químics i topogràfics de guiatge, en àrees grans i amb alts factors de multiplicació. A més, aquest copolímer de bloc ha demostrat l'obtenció de resultats d'auto-assemblatge dirigit molt exitosos, amb respecte a la seva capacitat d'integració.

- S'han dissenyat dos mètodes de guiatge químics basats en tècniques de litografia que no requereixen l'ús de resina. Aquests s'han implementat pel copolímer de bloc PS-*b*-PMMA. El patrons de guiatge han estat creats mitjançant la oxidació local de la superfície mitjançant litografia per AFM, i per mitjà de l'exposició directa de la superfície de polímer "brush" al feix d'electrons. El desenvolupament d'aquests mètodes, ha permès simplificar el nombre de passos de la seqüència del procés de fabricació, ja que no requereixen l'ús de resina. A més, permeten obtenir patrons de guiatge d'alta resolució.

- Per tal de millorar la resistència al gravat entre el PS i el PMMA, s'ha implementat un procés basat en la infiltració de materials per mitjà de la tècnica d'ALD. Aquest procés permet millorar el procés de transferència al substrat. S'ha demostrat pel sistema, PS-*b*-PMMA i per dos sistemes d'alta χ, amb dos materials d'infiltració diferents, Al_2O_3 i ZnO. La combinació d'aquesta tènica i la de guiatge dirigit mitjançant patrons topogràfics, s'ha aplicat al disseny i fabricació de raonadors nanomecànics per aplicacions de sensors de massa. Com que els nanofils són creats directament amb polímer infiltrat, l'avantatge del procés és que la mida d'aquests fils ve determinada per la meitat de la longitud de cadena del copolímer.

- S'han presentat dues tècniques per caracteritzar més profundament les pel·lícules primers de copolímers de bloc i les seves interaccions amb el substrat.

  S'ha demostrat que la tècnica HAXPES utilitzant radiació sincrotró, és una tècnica molt adequada per determinar i estudiar les propietats químiques de la superfície i interfícies en el procés d'auto-assemblatge dirigit.
  Mitjançant la caracterització de tres patrons de guiatge químics, s'han identificat les diferents modificacions químiques realitzades a la superfície del "brush". S'ha demostrat que quan el "brush" s'exposa a un plasma d'oxigen, es generat enllaços C-O, els quals promouen l'alta afinitat de la superfície al bloc de PMMA. En el cas de PON, s'ha observat la presència d'un òxid subestequiomètric entre la capa de "brush" i el substrat. Quan el polímer és exposat al feix d'electrons, hi ha un entrelligament de les molècules de PS, el qual indueix l'alineament del copolímer.

  La caracterització per AFM utilitzant el mode de *peak force quantitative nanomechanical mapping*, ha permès la caracterització de les propietats mecàniques de cadascun dels dominis del copolímer, sobrepassant les limitacions dels mètodes de nanoidentació estàndards. S'ha obtingut informació quantitativa sobre el mòdul de Young del PS i PMMA, al sistema PS-*b*-PMMA. Aquesta tècnica també s'ha aplicat a sistemes infiltrats, i ha permès reconèixer els canvis en la rigidesa dels materials induïts per la deposició i infiltració d'alúmina, així com l'evolució del gruix i rigidesa en funció del nombre de cicles d'ALD.

En resum, la recerca que s'ha dut a terme en el marc de la tesi, contribueix significativament a l'estudi de l'auto-assemblatge dirigit dels copolímers de bloc, ja que s'ha demostrat una implementació industrial factible per a un nou procés basat en epitàxia química. A més, s'ha realitzat un ampli estudi sobre la implementació i integració del procés amb nous materials. D'altra banda, s'ha presentat també el procés de fabricació d'un ressonador nanomecànic mitjançant la tècnica descrita i la tecnologia d'infiltració de materials.

Annexes

Annex I. Acronyms List

AFM	Atomic force microscopy
ALD	Atomic layer deposition
ARC	Antireflective coating
ATRP	Atom-transfer polymerization
BA	Butylacetate
BCP	Block copolymer
CAR	Chemically amplified resist
CD	Critical dimension
CMOS	Complementary metal–oxide–semiconductor
CVD	Chemical vapor deposition
DEZ	Diethylzinc
DGL	Ginzburg-Landau theory
DMT	Derjaguin-Muller-Toporov
DPP	Discharge produced plasma
DSA	Directed self-assembly
DUV	Deep ultraviolet
EBL	Electron beam lithography
EUV	Extreme ultraviolet
FEM	Focus Energy matrix
FFT	Fast Fourier Transform
FIB	Focused ion beam

GISAXS	Grazing-incidence small-angle X-ray scattering
HAXPES	Hard X-ray high kinetic energy photoelectron spectroscopy
HF	Hydrofluoric acid
hPS	Homopolymer polystyrene
HSP	Hansen solubility parameters
IC	Integrated circuit
ICP	Inductively coupled plasma
IL	Interference lithography
IPA	Isopropanol
ITRS	International technology roadmap for semiconductors
LAO	Local anodic oxidation
LER	Line edge roughness
LPP	Laser produced plasma
LWR	Line width roughness
MEMS	Micro electromechanical system
MIBK	Methyl isobutyl ketone
NA	Numerical aperture
NEMS	Nano electromechanical system
NGL	Next generation lithography
NIL	Nanoimprint lithography
NMP	Nitroxide-mediated polymerization
NMR	Nuclear Magnetic Resonance spectroscopy
ODT	Order-disorder transition

OTS	Octadecyltrichlorosilane
OWRK	Owens, Wendt, Rabel and Kaelble
PDI	Polydispersity index
PDMS	Polydimethylsiloxane
PGMEA	propylene glycol monomethyl ether acetate
PLA	Polylactide acid
PLA-*b*-PDMS-*b*-PLA	poly(dimethylsiloxane)-*b*-poly(lactic acid)
PMMA	Polymethyl methacrylate
PON	Parallel Oxidation Nanolithography
PS	Polystyrene
PS-*b*-PB	Poly(styrene-*b*-butadiene)
PS-*b*-PEO	Poly(styrene-b-ethylene oxide)
PS-*b*-PLA	Poly(styrene-*b*-D,L-lactide)
PS-*b*-PMMA	Poly(styrene-*b*-methyl methacrylate)
PS-OH	Hydroxyl terminated polystyrene
PS-*r*-PMMA-OH	Random hydroxyl terminated poly(styrene-*b*-methyl methacrylate)
QNM	Quantitative nanomechanical mapping
RAFT	Reversible addition-fragmentation chain transfer
RED	Relative energy difference
RIE	Reactive ion etching
SAM	Self-assembled monolayer
SAXS	Small angle X-ray scattering
SCFT	Self-consistent field theory

SEC	Size Exclusion Chromatography
SEM	Scanning electron microscopy
SIS	Sequential infiltration synthesis
SOC	Spin-on-carbon
SPL	Scanning probe lithography
SPM	Scanning probe microscopy
SSL	Strong segregation limit
STM	Scanning tunneling microscopy
TBD	triazabicyclodecene
TMA	Trimethylaluminum
WSL	Weak segregation
XPS	X-Ray Photoelectron Spectroscopy
X-PS	Cross-linkable polystyrene

Annex 2. Scientific contributions

List of publications

Laura Evangelio, Marta Fernández Regúlez, Xavier Borrisé, Matteo Lorenzoni, Jordi Fraxedas, Francesc Pérez Murano, *"Creation of guiding patterns for directed self-assembly of block copolymers by resistless direct e-beam exposure"*, J. Micro/Nanolith. MEMA MOEMS, 14 (3)m 033511 (2015)

Marta Fernández Regúlez, Laura Evangelio, Matteo Lorenzoni, Jordi Fraxedas, Francesc Pérez Murano, *"Sub-10 nm resistless nanolithography for directed self-assembly of block copolymers"*, ACS Applied Materials & Interfaces, 6 (23), 21596-21602 (2014)

Matteo Lorenzoni, Laura Evangelio, Marta Fernández-Regúlez, Célia Nicolet, Christophe Navarro, Francesc Pérez-Murano, *"Sequential Infiltration of Self-Assembeld Block Copolyners: AStudy by Atomic Force Microscopy"*, J. Phys. Chem. C, 121, 3078-3086 (2017)

Matteo Lorenzoni, Laura Evangelio, Sophie Verhaeghe, Célia Nicolet, Christophe Navarro, Francesc Pérez-Murano, *"Assessing the local nanomechanical properties of self-assembled block co-polymers thin films by peak force tapping"*, Langmuir, 31 (42) 11630-11638 (2015)

Matteo Lorenzoni, Laura Evangelio, Sophie Verhaeghe, Célia Nicolet, Christophe Navarro, Alvaro San Paulo, Gemma Rius, Francesc Pérez-Murano, *"Nanomechanical properties of solvent cast PS and PMMA polymer blends and block copolymers"*, J. Micro/Nanolith. MEMS MOEMS, 14 (3)m 033509, (2015)

Currently, there are more articles in preparation.

Conference contributions

"Use of ALD Sequential Infiltration Synthesis to improve the pattern transfer on Directed Self-Assembly high-chi PS-b-PLA block copolymers"

Laura Evangelio, Marta Fernández-Regúlez, Xavier Chevalier, Celia Nicolet, Ian Cayrefourcq, Christophe Navarro and Francesc Pérez-Murano

SPIE Advanced Lithography 2017, February 2017, San Jose, California (EEUU)

Oral Presentation

"Control of interface energies for implementing directed self-assembly of block copolymers in a 300 mm CMOS processing line"

Laura Evangelio, Marta Fernández-Regúlez, Patricia Pimenta-Barros, Maxime Argoud, Xavier Chevalier, Celia Nicolet, Ian Cayrefourcq, Christophe Navarro, Raluca Tiron, Marcus Müller and Francesc Pérez-Murano

SPIE Advanced Lithography 2017, February 2017, San Jose, California (EEUU)

Poster Presentation

"Control of interface energies for implementing directed self-assembly of block copolymers in a 300 mm CMOS processing line"

Laura Evangelio, Marta Fernández-Regúlez, Patricia Pimenta-Barros, Maxime Argoud, Xavier Chevalier, Celia Nicolet, Ian Cayrefourcq, Christophe Navarro, Raluca Tiron, Marcus Müller and Francesc Pérez-Murano

2nd DSA Symposium, October 2016, Grenoble (France)

Oral Presentation

"Use of atomic layer deposition for improving pattern transfer in directed self-assembly of PS-b-PMMA"

Laura Evangelio, Matteo Lorenzoni, Marta Fernández-Regúlez, Steven Gottlieb, Francesc Pérez-Murano

SR-ALD Workshop, ALBA Synchrotron, June 2016, Cerdanyola del Vallès (Spain)

Oral Presentation

"Use of atomic layer deposition for improving pattern transfer in directed self-assembly of PS-b-PMMA"

Laura Evangelio, Matteo Lorenzoni, Marta Fernández-Regúlez, Steven Gottlieb, Francesc Pérez-Murano

Nanoselect, June 2016, Sant Feliu de Guíxols (Spain)

Oral presentation

"Role of interface energies in the directed self-assembly of block copolymers in wide chemical patterns"

Laura Evangelio, Weihua Li, Matteo Lorenzoni, Jordi Fraxedas, Marcus Müller and Francesc Pérez-Murano

EUPOC 2016 on Block copolymers, May 2016, Lago di Garda (Italy)

Oral presentation

"Creation of chemical guiding patterns for DSA of block copolymers by high resolution resistless nanolithography methods"

Laura Evangelio, Marta Fernández-Regúlez, Xavier Borrisé, Matteo Lorenzoni, Jordi Fraxedas, Francesc Pérez-Murano

1st International Symposium on DSA, October 2015, Leuven (Belgium)

Poster presentation

"Enabling density multiplication in directed self-assembly of block copolymers by chemical surface modification using wide guiding stripes"

Laura Evangelio, Weihua Li, Matteo Lorenzoni, Marcus Müller, Francesc Pérez-Murano

1st International Symposium on DSA, October 2015, Leuven (Belgium)

Poster presentation

"Determination of the interfacial energies in chemical guiding patterns for directed self-assembly of block co-polymers"

Laura Evangelio, Matteo Lorenzoni, Jordi Fraxedas, Francesc Pérez-Murano

International Conference on Micro and Nano Engineering (MNE), September 2015, The Hague (Netherlands)

Oral presentation

"Characterization of buried interfaces of grafted polymer films using high kinetic energy photoemission"

Laura Evangelio, Matteo Lorenzoni, Federico Gramazio, Francesc Pérez-Murano, Jordi Fraxedas

II ALBA User's Meeting, June 2015, Barcelona (Spain)

Poster presentation

"Assessing the local nanomechanical properties of self-assembled block copolymers thin films by Peak Force tapping."

Matteo Lorenzoni, Laura Evangelio, Célia Nicolet, Christophe Navarro, Francesc Pérez-Murano

European Conference on Surface Science, September 2015, Barcelona (Spain)

Oral presentation

"Characterization of buried interfaces of grafted polymer films using high kinetic energy photoemission"

Laura Evangelio, Matteo Lorenzoni, Federico Gramazio, Francisco Espinosa, Ricardo García, Francesc Pérez-Murano, Jordi Fraxedas

European Conference on Surface Science, September 2015, Barcelona (Spain)

Oral presentation

"Directed self-assembly of block copolymers by chemical surface modification"

Laura Evangelio, Marta Fernández-Regúlez, Matteo Lorenzoni, Francesc Pérez-Murano, Jordi Fraxedas

1st Scientific Meeting of BNC-b Students, May 2015, Barcelona (Spain)

Oral Presentation

"Formation of chemical guiding patterns for DSA of block copolymers by high resolution resistless nanolithography methods"

Laura Evangelio, Marta Fernández-Regúlez, Xavier Borrisé, Matteo Lorenzoni, Jordi Fraxedas, Francesc Pérez-Murano

European Materials Research Society, May 2015, Lille (France)

Oral presentation

"Enabling density multiplication in directed self-assembly of block copolymers by chemical surface modification using wide guiding stripes"

Laura Evangelio, Weihua Li, Matteo Lorenzoni, Marcus Müller, Francesc Pérez-Murano

European Materials Research Society, May 2015, Lille (France)

Oral presentation

"Nanomechanical properties of different phases in assembled block copolymers thin films"

Matteo Lorenzoni, Laura Evangelio, Célia Nicolet, Christophe Navarro, Alvaro San Paulo, Francesc Pérez-Murano

European Materials Research Society, May 2015, Lille (France)

Poster presentation

"Creation of guiding patterns for directed self-assembly of block co-polymers by resistless direct e-beam exposure"

Laura Evangelio, Marta Fernández-Regúlez, Xavier Borrisé, Matteo Lorenzoni, Jordi Fraxedas, Francesc Pérez-Murano

SPIE Advanced Lithography 2015, February 2015, San Jose, California (EEUU)

Poster presentation

"Challenges and opportunities of scanning probe lithography for creation of guiding patterns used in directed self-assembly of block co-polymers"

Laura Evangelio, Matteo Lorenzoni, Marta Fernández-Regúlez, Marcus Kaesner, Yana Krivoshapkina, Ivo W. Rangelow, Francesc Pérez-Murano

SPIE Advanced Lithography 2015, February 2015, San Jose, California (EEUU)

Oral presentation

"Nanomechanical properties of solvent cast PS and PMMA polymer blends and block co-polymers"

Matteo Lorenzoni, Laura Evangelio, Celia Nicolet, Christophe Navarro, Francesc Pérez-Murano

SPIE Advanced Lithography 2015, February 2015, San Jose, California (EEUU)

Poster presentation

"Density multiplication in directed self-assembly of block co-polymers by chemical surface modification using wide guiding stripes"

Laura Evangelio, Marta Fernández-Regúlez, Weihua Li, Matteo Lorenzoni, Jordi Fraxedas, Marcus Müller, Francesc Pérez-Murano

SPIE Advanced Lithography 2015, February 2015, San Jose, California (EEUU)

Poster presentation

"Directed Self-Assembly of block copolymers by chemical surface modification"
Laura Evangelio, Marta Fernández-Regúlez, Jordi Fraxedas, Francesc Pérez-Murano
Nanolito Workshop in Nanolithography, October 2014, Zaragoza (Spain)
Oral presentation

"AFM nanolithography for block copolymer directed self-assembly"
Laura Evangelio, Marta Fernández-Regúlez, Jordi Fraxedas, Francesc Pérez-Murano
European Conference on Surface Science, September 2014, Antalya (Turkey)
Oral presentation

"AFM nanolithography for block copolymer directed self-assembly"
Laura Evangelio, Marta Fernández-Regúlez, Jordi Fraxedas, Francesc Pérez-Murano
1st SNM Workshop, July 2014, Barcelona (Spain)
Oral presentation

"Creation of chemical guiding patterns for directed self-assembly of block co-polymers by AFM lithography"
Laura Evangelio, Marta Fernández-Regúlez, Jordi Fraxedas, Francesc Pérez-Murano
SPIE Advanced Lithography 2014, February 2014, San Jose, California (EEUU)
Poster Presentation

"Block co-polymer multiple patterning direct self-assembly on PS-OH brush layer and AFM based nanolithography"
Marta Fernández-Regúlez, Laura Evangelio, Jordi Fraxedas, Francesc Pérez-Murano
Nanoimprint and Nanoprint Technology 2013, October 2013, Barcelona (Spain)
Poster Presentation

"AFM nanolithography for creating guiding patterns for directed self-assembly of block co-polymers"
Marta Fernández-Regúlez, Laura Evangelio, Jordi Fraxedas, Francesc Pérez-Murano
International Conference on Micro and Nano Engineering 2013, London (United Kingdom)
Oral Presentation

"Block co-polymer multiple patterning direct self-assembly on PS-OH brush layer and AFM based nanolithography"
Marta Fernández-Regúlez, Laura Evangelio, Jordi Fraxedas, Francesc Pérez-Murano
Euronanoforum 2013, CRANN/Intel DSA Workshop , June 2013, Dublin (Ireland)
Oral Presentation